nature materials

Supplementary information

https://doi.org/10.1038/s41563-024-02011-x

A family of dual-anion-based sodium superionic conductors for all-solid-state sodium-ion batteries

In the format provided by the authors and unedited

Table of contents:

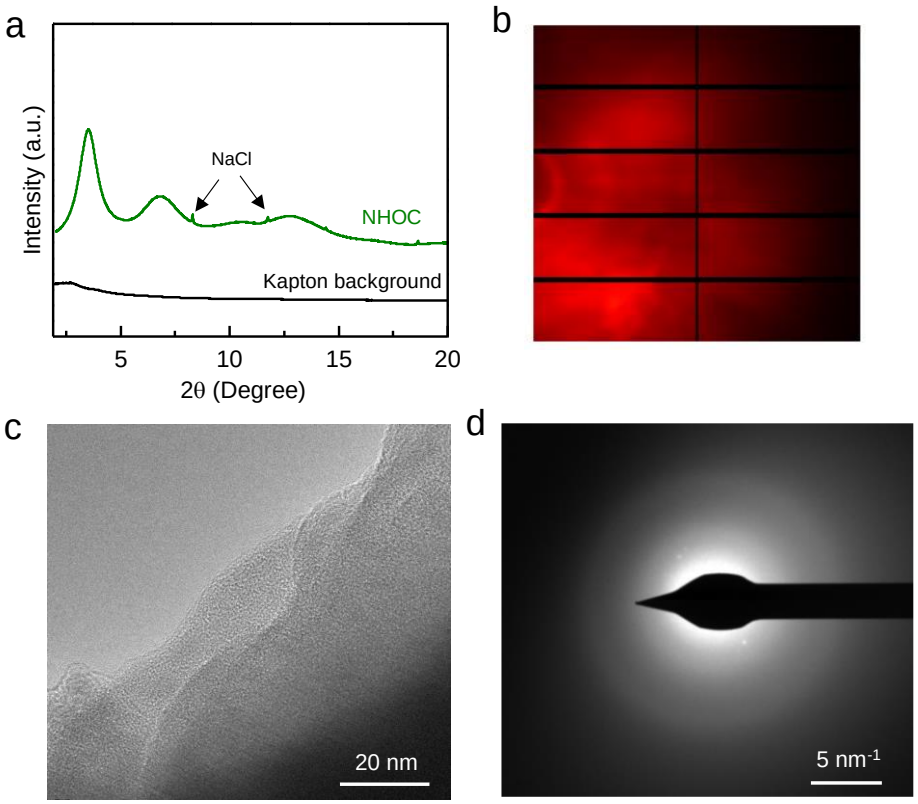

Supplementary Fig. 1. Synchrotron-based (a) XRD and (b) 2D diffraction pattern of as-prepared NHOC. (c) High-resolution TEM image and (d) selected area electron diffraction (SAED) pattern of NHOC sample.

The wide diffraction peaks of synchrotron XRD at $2\theta = 3.5°$, 6.8°, and 12.8° indicate an amorphous state of NHOC, with negligible amount of NaCl impurity can be detected. The TEM image and SAED diffraction pattern are consistent with the XRD results, which further validates the amorphous nature of the obtained NHOC.

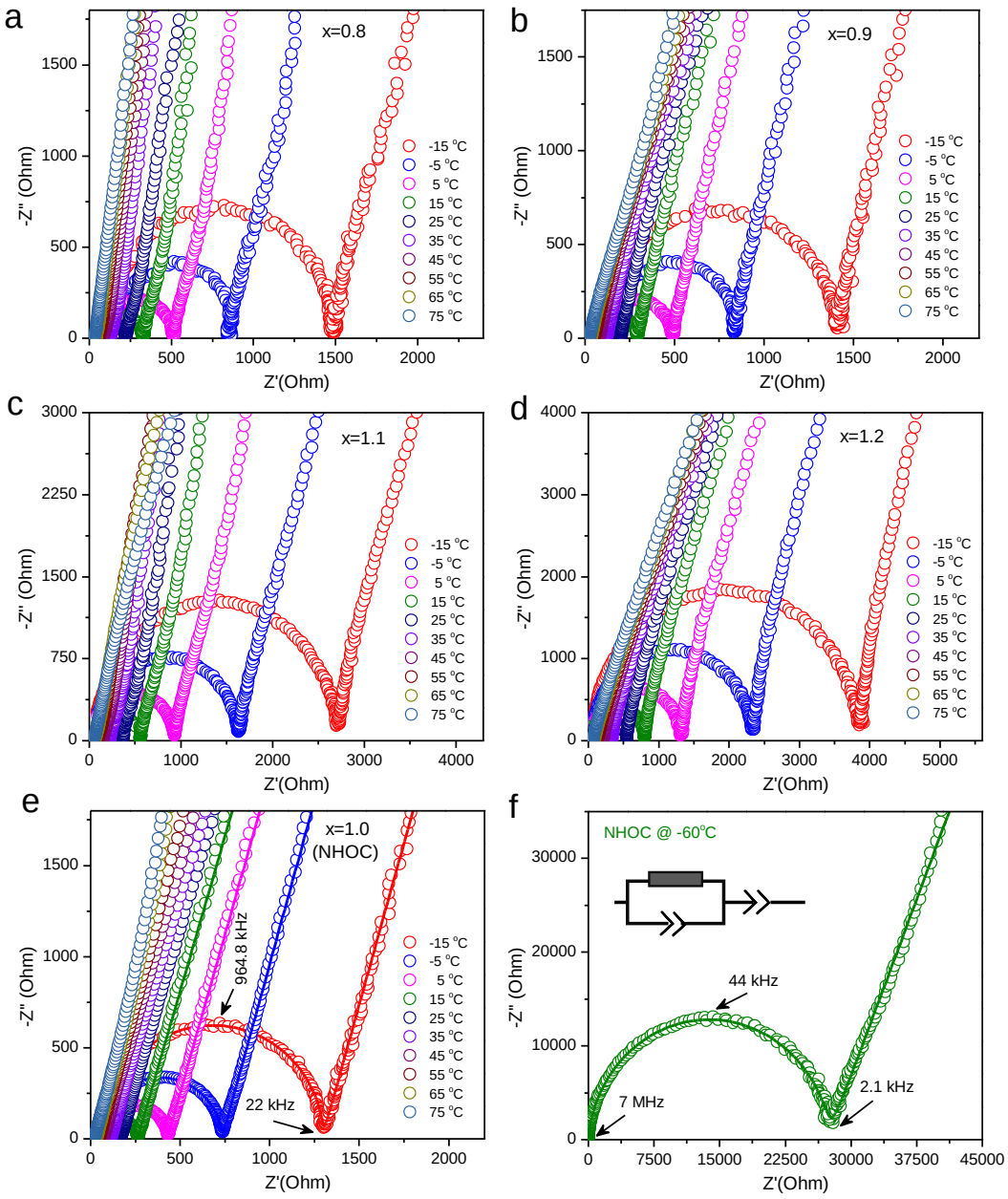

Supplementary Fig. 2. **Nyquist plots of as-prepared samples.** (a-e) Nyquist plots of xNa_2O_2-$HfCl_4$ ($0.8 \leq x \leq 1.2$) samples at different temperatures. (f) The Nyquist plot of amorphous NHOC at -60°C. Inset is the equivalent circuit model for the fitting of Nyquist plot at -60°C.

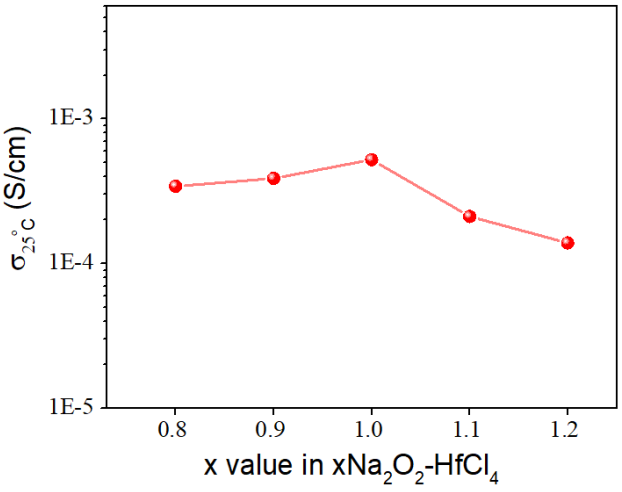

Supplementary Fig. 3. The ionic conductivities of xNa_2O_2-$HfCl_4$ ($0.8 \leq x \leq 1.2$) samples at 25°C.

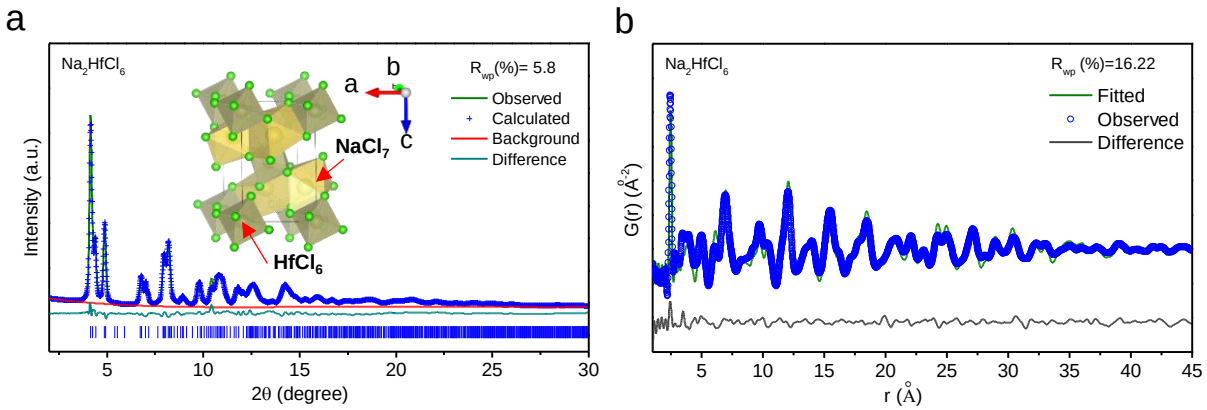

Supplementary Fig. 4. (a) The synchrotron-based XRD pattern of Na_2HfCl_6 and the corresponding Rietveld refinements. Insert is the crystal structure of Na_2HfCl_6. (b) The fitted synchrotron PDF profile of Na_2HfCl_6 electrolyte. The Na_2HfCl_6 was synthesized with the same procedure to that of the NHOC electrolyte.

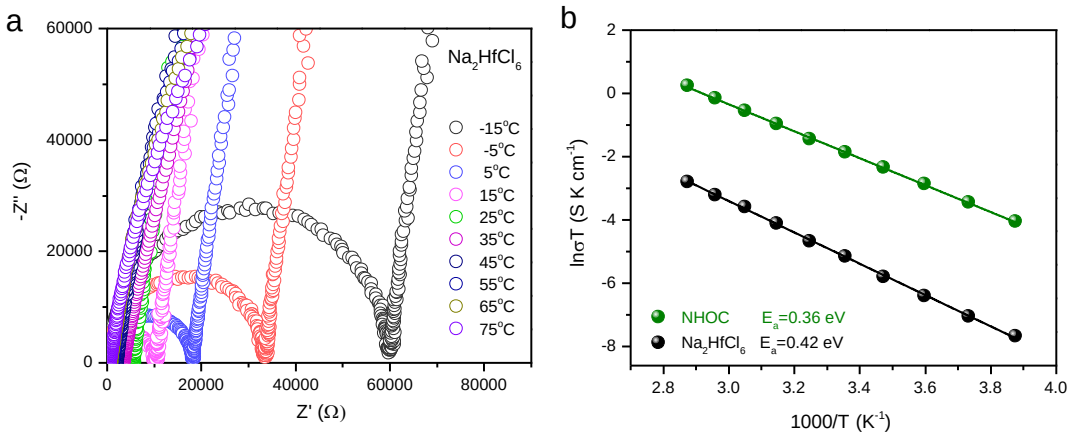

Supplementary Fig. 5. (a) Nyquist plots of Na_2HfCl_6 electrolyte at different temperatures. (b) The Arrhenius plots of the NHOC and Na_2HfCl_6 electrolytes.

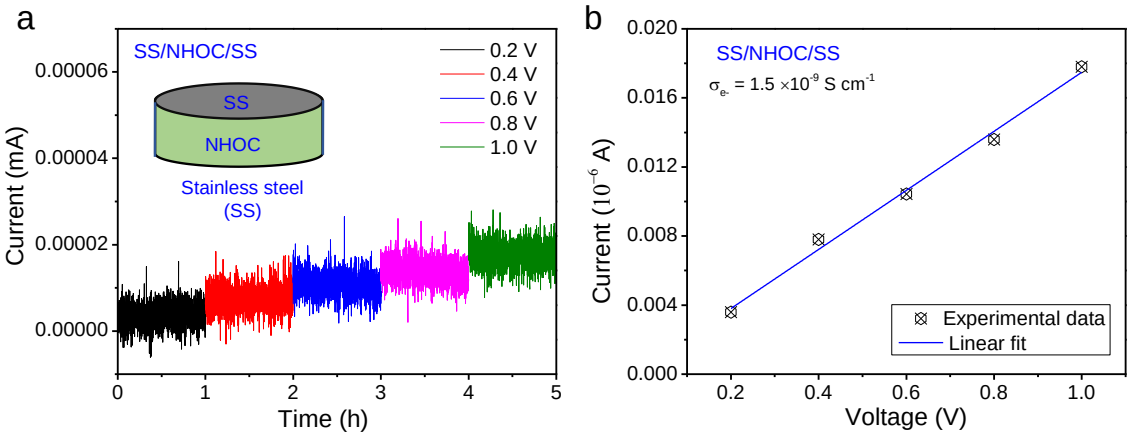

Supplementary Fig. 6. DC polarization curves of the NHOC electrolyte using ion-blocking symmetric cell at different voltages. (b) Equilibrium current responses at different applied voltages.

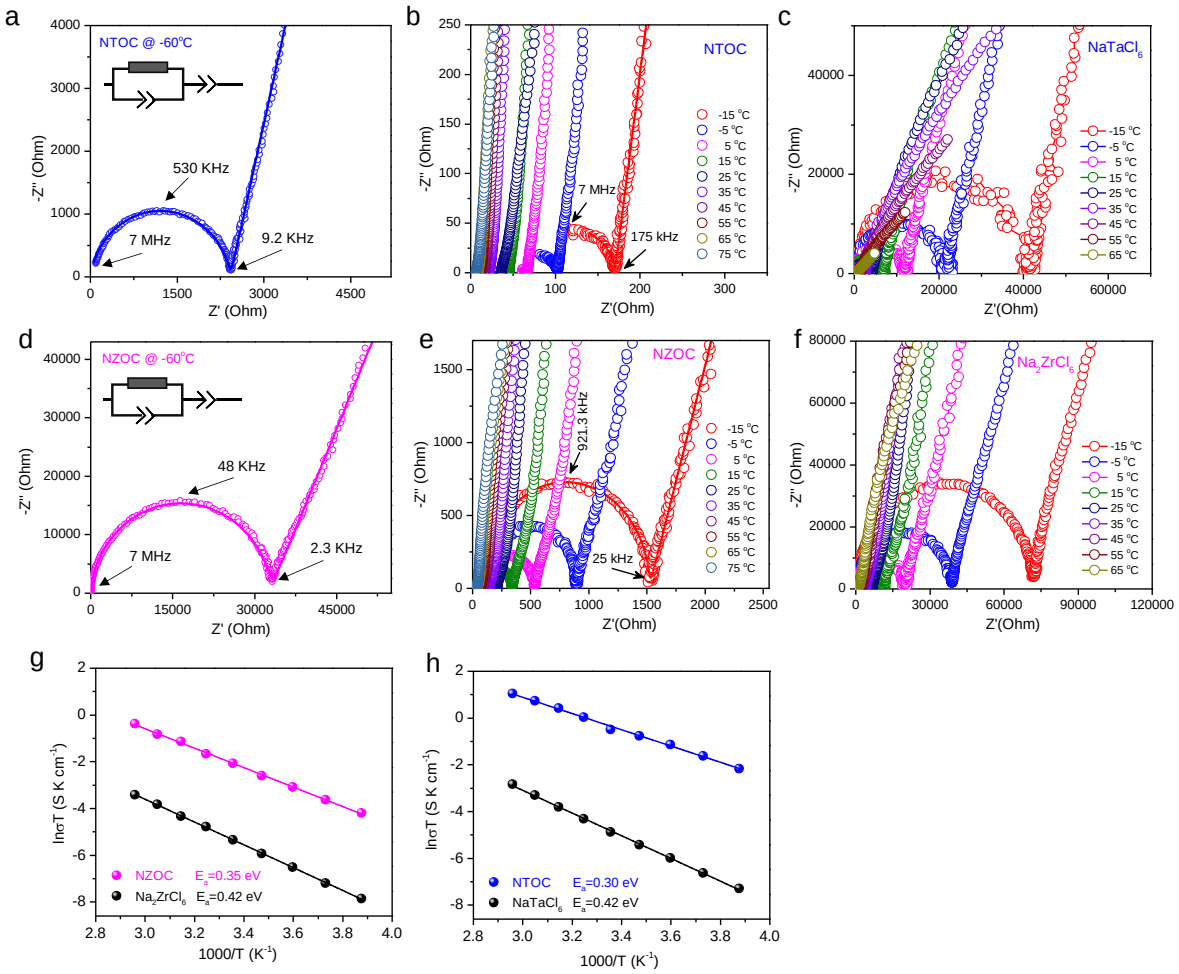

Supplementary Fig. 7. Nyquist plots of (a, b) NTOC and (c) $NaTaCl_6$ electrolytes at different temperatures. Nyquist plots of (d, e) NZOC and (f) Na_2ZrCl_6 electrolytes at different temperatures. Inset are the equivalent circuit model for the fitting of Nyquist plot at -60°C. (g) The Arrhenius plots of the NZOC and Na_2ZrCl_6 electrolytes. (h) The Arrhenius plots of the NTOC and $NaTaCl_6$ electrolytes.

The fitted Nyquist plots of amorphous NTOC and NZOC at -60°C suggests their high bulk ionic conductivities without grain boundary response.

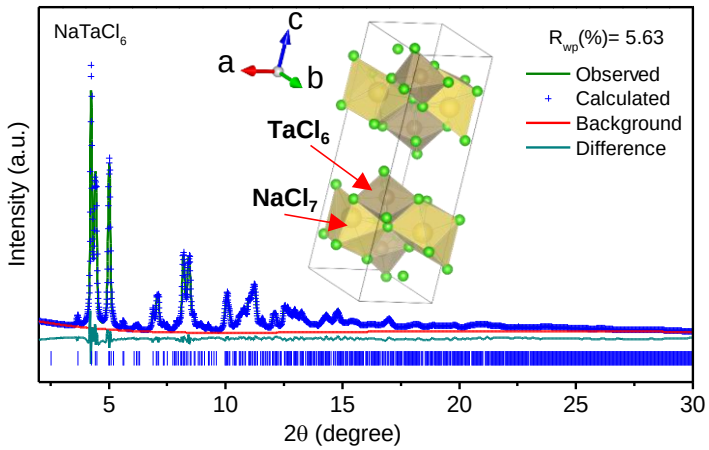

Supplementary Fig. 8. The synchrotron-based XRD pattern of $NaTaCl_6$ and the corresponding Rietveld refinements. Insert is the crystal structure of $NaTaCl_6$.

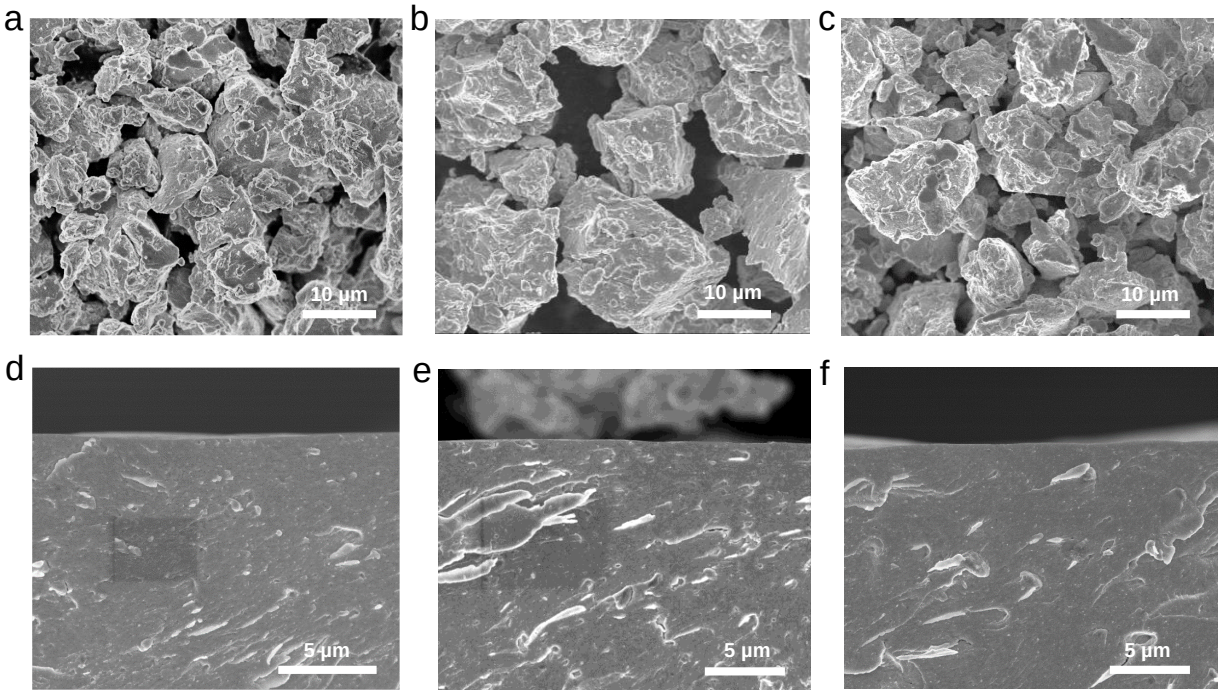

Supplementary Fig. 9. The SEM images of as-prepared (a) NHOC, (b) NZOC, and (c) NTOC electrolyte powder. Cross-sectional SEM images of cold-pressed (d) NHOC, (e) NZOC, and (f) NTOC electrolyte pellets at ~ 400 MPa.

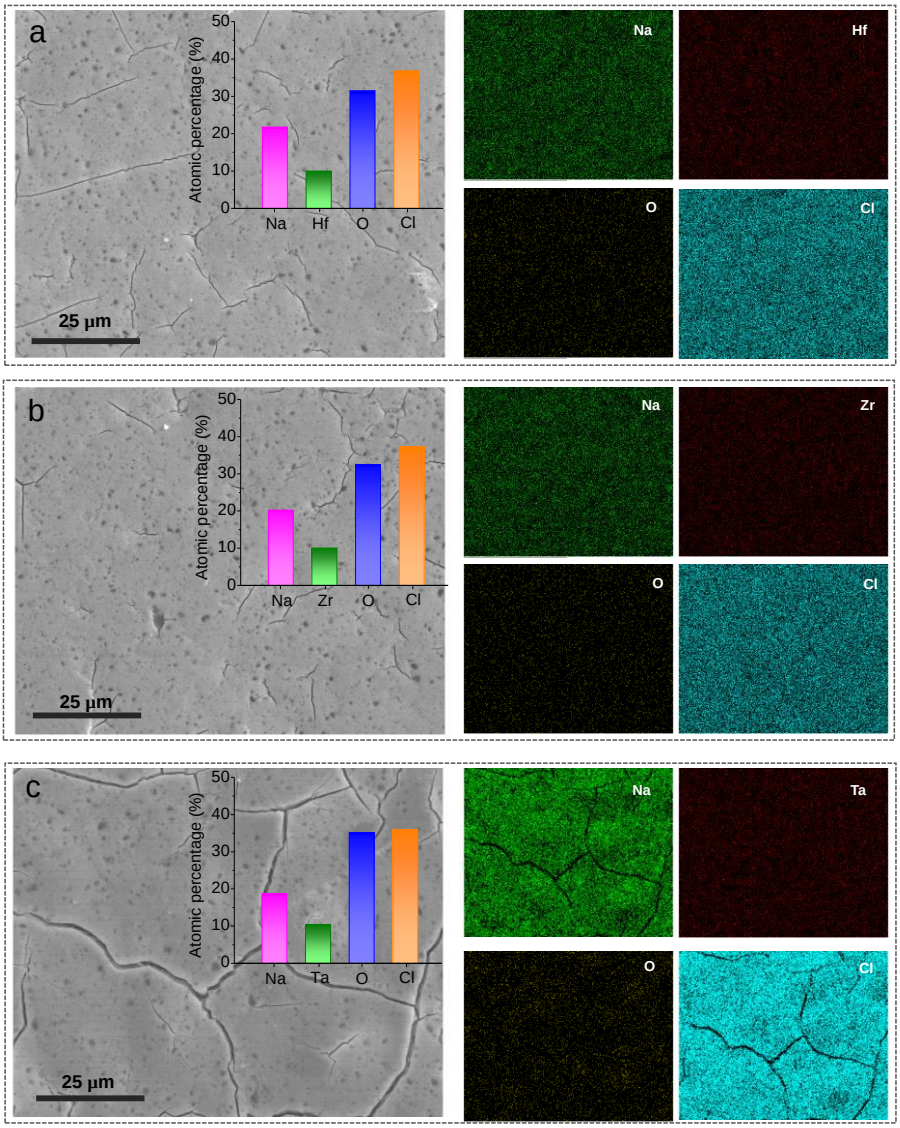

Supplementary Fig. 10. Backscattered electron images and the corresponding energy dispersive X-ray spectroscopy (EDS) elemental mapping for the surface of cold-pressed (a) NHOC, (b) NZOC, and (c) NTOC electrolytes.

The large cracks appeared in the electrolytes were result from high stress encountered during demolding. The oxygen content in NMOC electrolytes being off-stoichiometric because the light element content cannot be detected precisely. However, based on the atomic percentage of Na, M, and Cl in NMOC and the theory of charge neutrality balancing, it can be conclued that the atomic percentage of O in NMOC is slightly different.

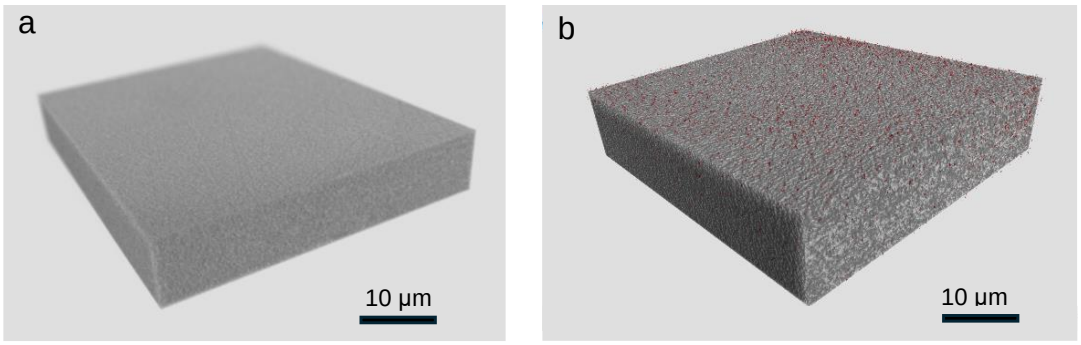

Supplementary Fig. 11. The 3D volume rendered images from the synchrotron-based X-ray computed tomography (CXT) of cold-pressed (a) NHOC and (b) Na_2HfCl_6 electrolytes at ~ 400 MPa.

The images present the virtual images of electrolyte and cracks/voids together. The gray represents solid electrolyte and red represents the cracks and voids. The cold-pressed electrolyte pellets were left inside the mold for direct XCT characterization to avoid the large cracks induced by external stress encountered during the demolding process.

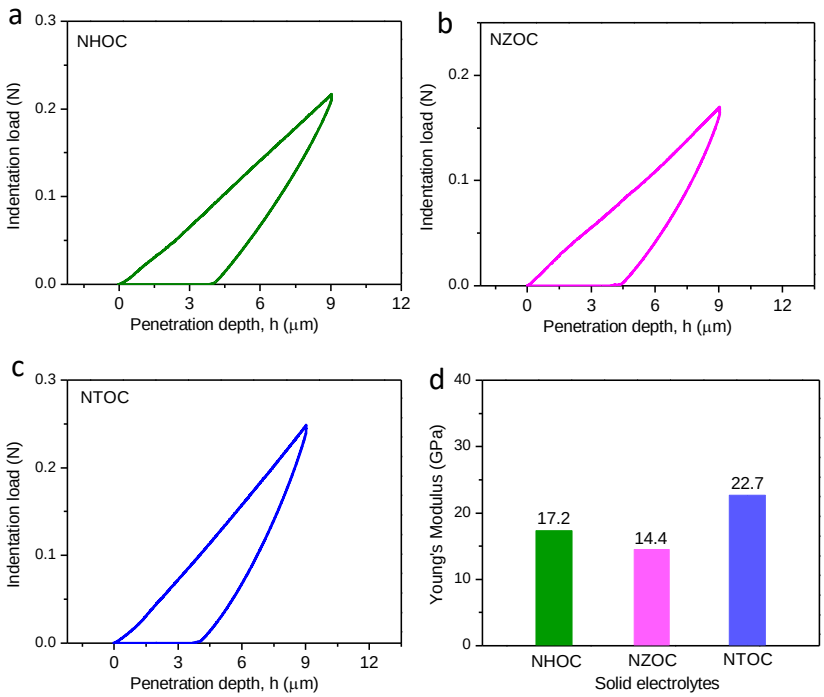

Supplementary Fig. 12. (a-c) Load-displacement response of the NMOC SSEs upon nanoindentations. (d) Young's modulus of NHOC, NZOC, and NTOC electrolytes.

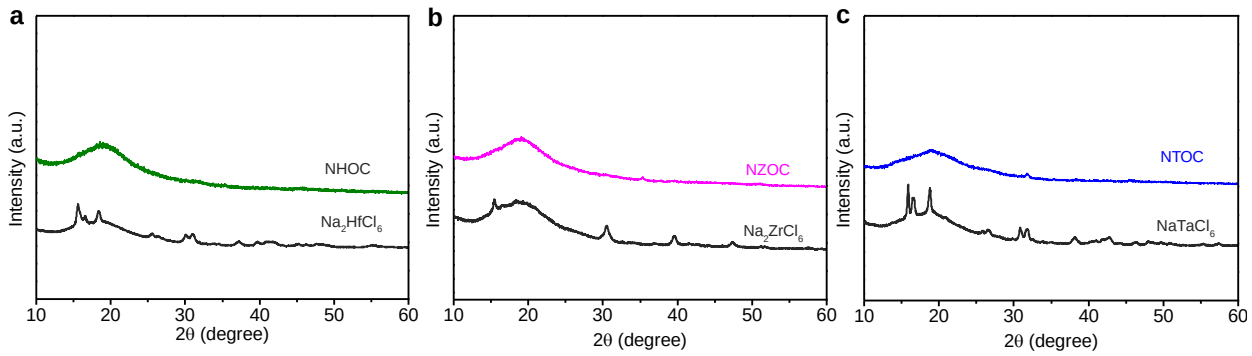

Supplementary Fig. 13. Lab-based XRD patterns of Na_2HfCl_6, Na_2ZrCl_6, and $NaTaCl_6$ SSEs synthesized with the same procedure to that of the NMOC SSEs.

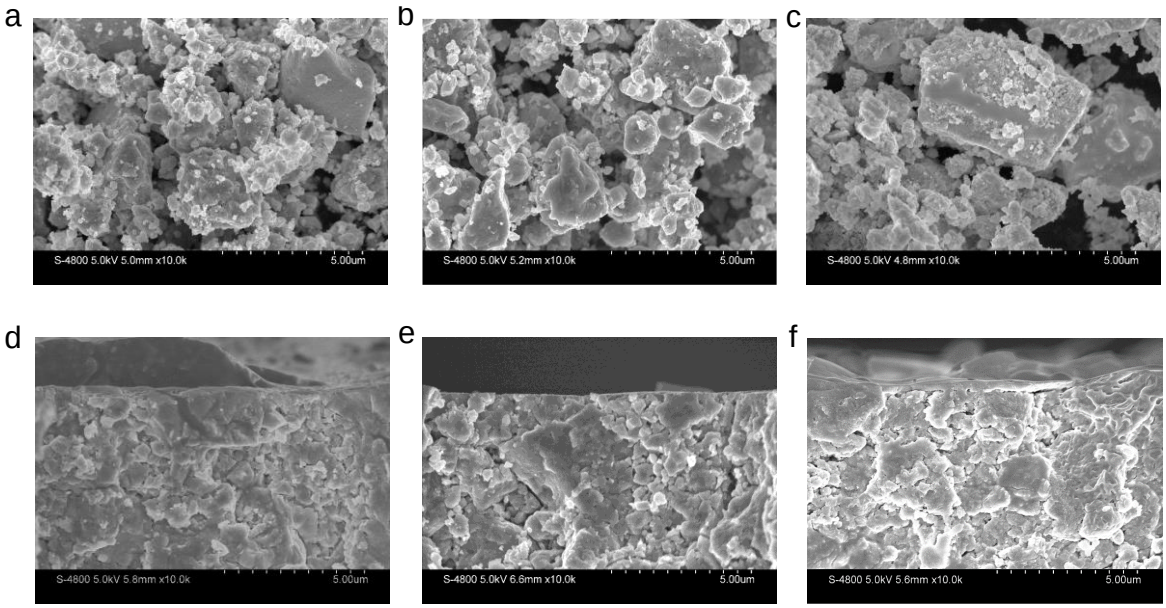

Supplementary Fig. 14. The SEM images of as-prepared (a) Na_2HfCl_6, (b) Na_2ZrCl_6, and (c) $NaTaCl_6$ SSEs. Cross-sectional SEM images of cold-pressed (d) Na_2HfCl_6, (e) Na_2ZrCl_6, and (f) $NaTaCl_6$ SSEs at ~ 400 MPa.

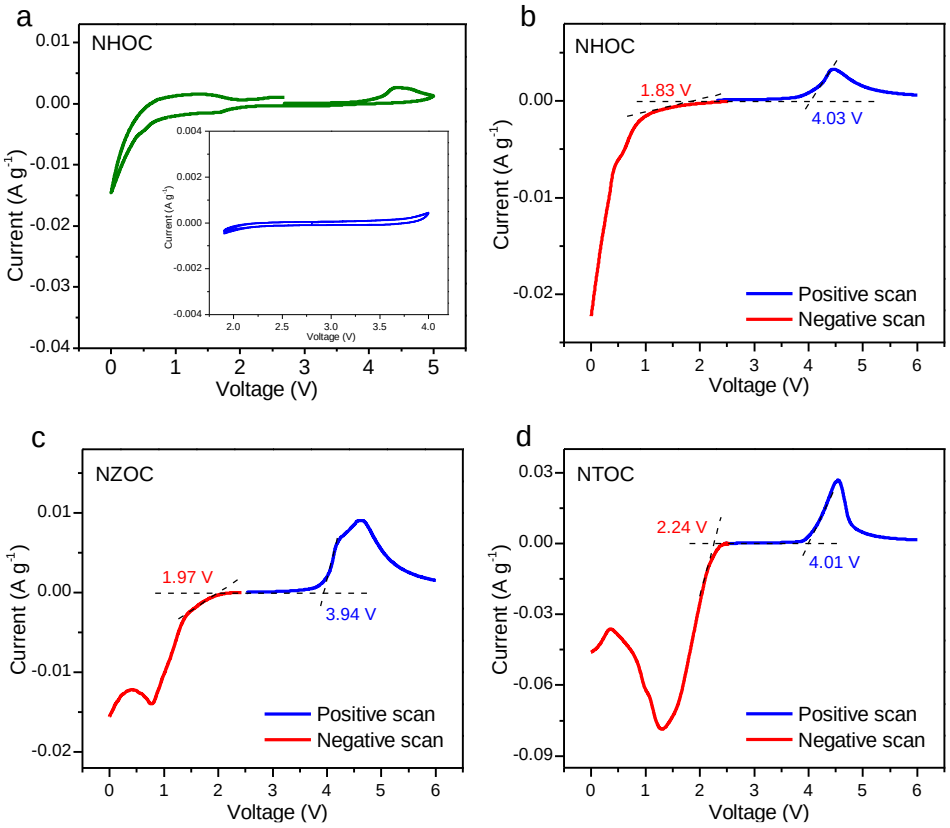

Supplementary Fig. 15. (a) CV profile of the NHOC SSE in 0-5 V (*vs.* $Na^+/Na_{15}Sn_4$) at a scan rate of 0.1 mV S^{-1} (insert is the CV profile of the NHOC SSE between 1.9 and 4 V (*vs.* $Na^+/Na_{15}Sn_4$) at a scan rate of 0.1 mV S^{-1}). The LSV profiles of (b) NHOC, (c) NZOC, and (d) NTOC SSEs at a scan rate of 0.1 mV S^{-1}.

The high oxidation stability is intrinsic to the oxychloride anion chemistry, while the low voltage limits are attributed to the reduction of high-valence $M^{4+/5+}$ components.[1,2]

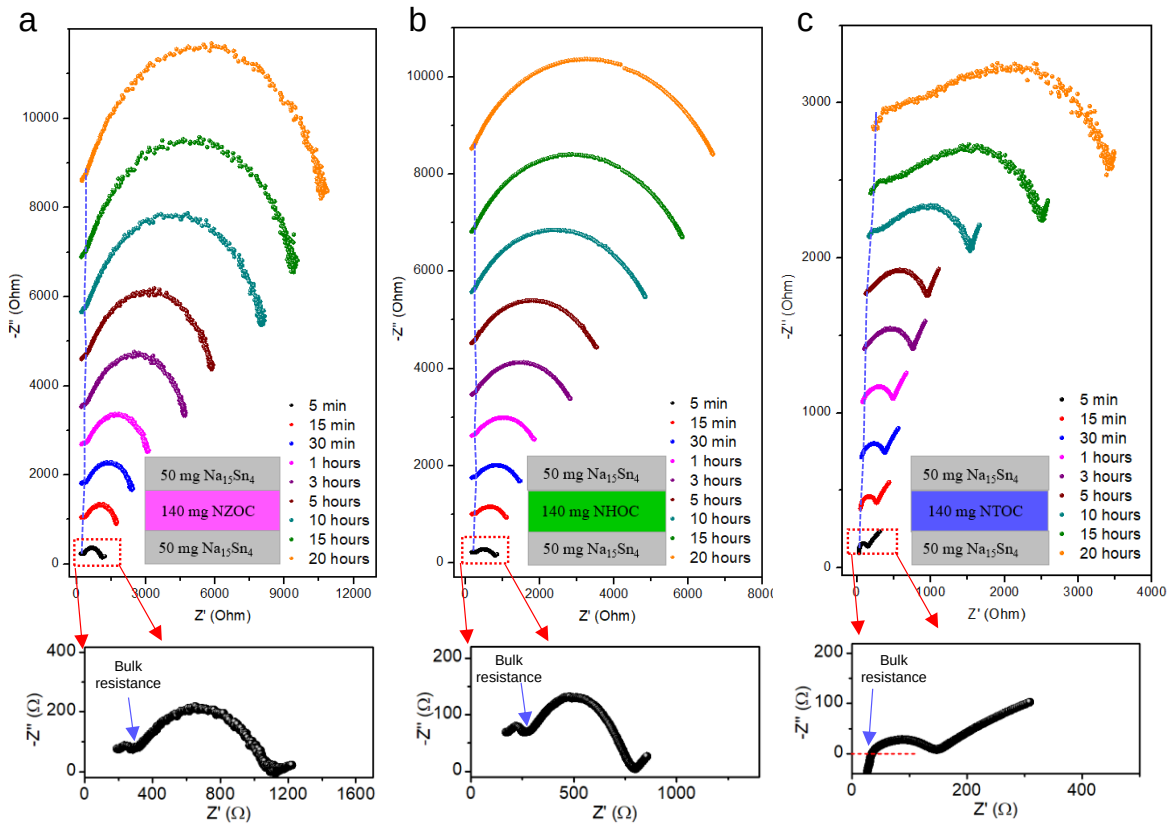

Supplementary Fig. 16. Time-resolved EIS spectra of (a) $Na_{15}Sn_4$/NZOC/$Na_{15}Sn_4$, (b) $Na_{15}Sn_4$/NHOC/$Na_{15}Sn_4$, and (c) $Na_{15}Sn_4$/NTOC/$Na_{15}Sn_4$ symmetric cells at room temperature. Frequency: 2 MHz-1000 mHz.

The amorphous NMOC SSEs react with $Na_{15}Sn_4$ electrode spontaneously without electrochemical process, as verified by the appearance of a second semicircle at the middle frequency. Moreover, the semicircle at the middle frequency enlarged significantly with the time increase, suggesting the generation of non-passivating interphases between the NMOC SSEs and $Na_{15}Sn_4$ anode.

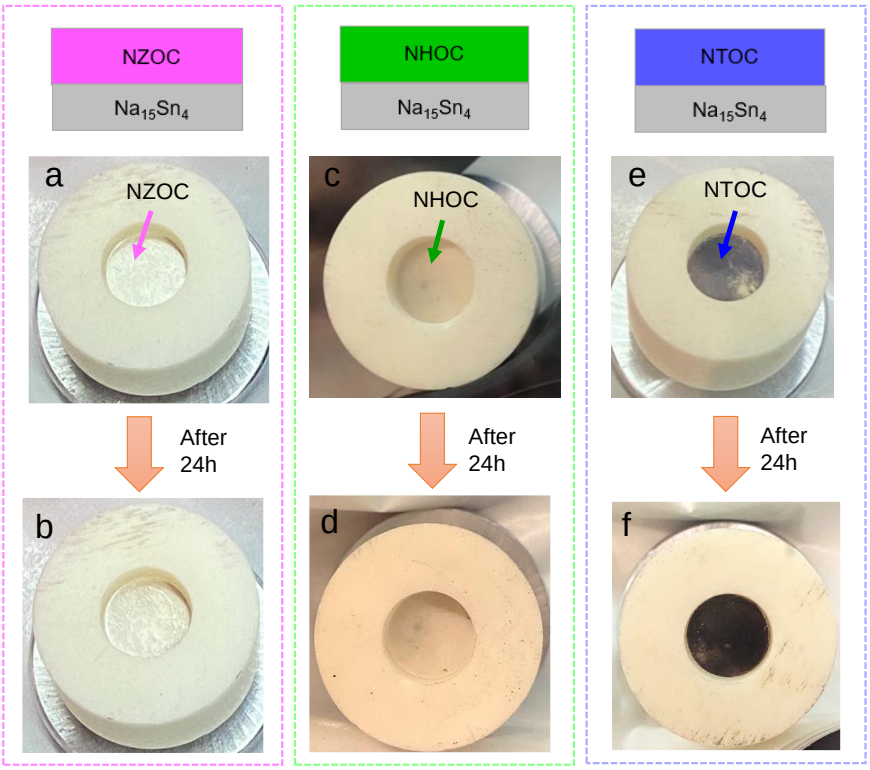

Supplementary Fig. 17. The photographs of NZOC electrolyte after cold press with $Na_{15}Sn_4$ for (a) 0h and (b) 24h; the photographs of NHOC electrolyte after cold press with $Na_{15}Sn_4$ for (c) 0h and (d) 24h; The photographs of NTOC electrolyte after cold press with $Na_{15}Sn_4$ for (e) 0h and (f) 24h.

The color of the NTOC SSE pellet changed from pale yellow to black momentarily after simple cold-pressed with $Na_{15}Sn_4$, which visually demonstrated the generation of non-passivating interphase and the reaction front rapidly propagates into the bulk NTOC SSE. Negligible color changes can be observed for NHOC and NZOC SSEs after resting for 24h, suggesting relative slower interfacial reaction kinetics compared with these of the NTOC electrolyte.

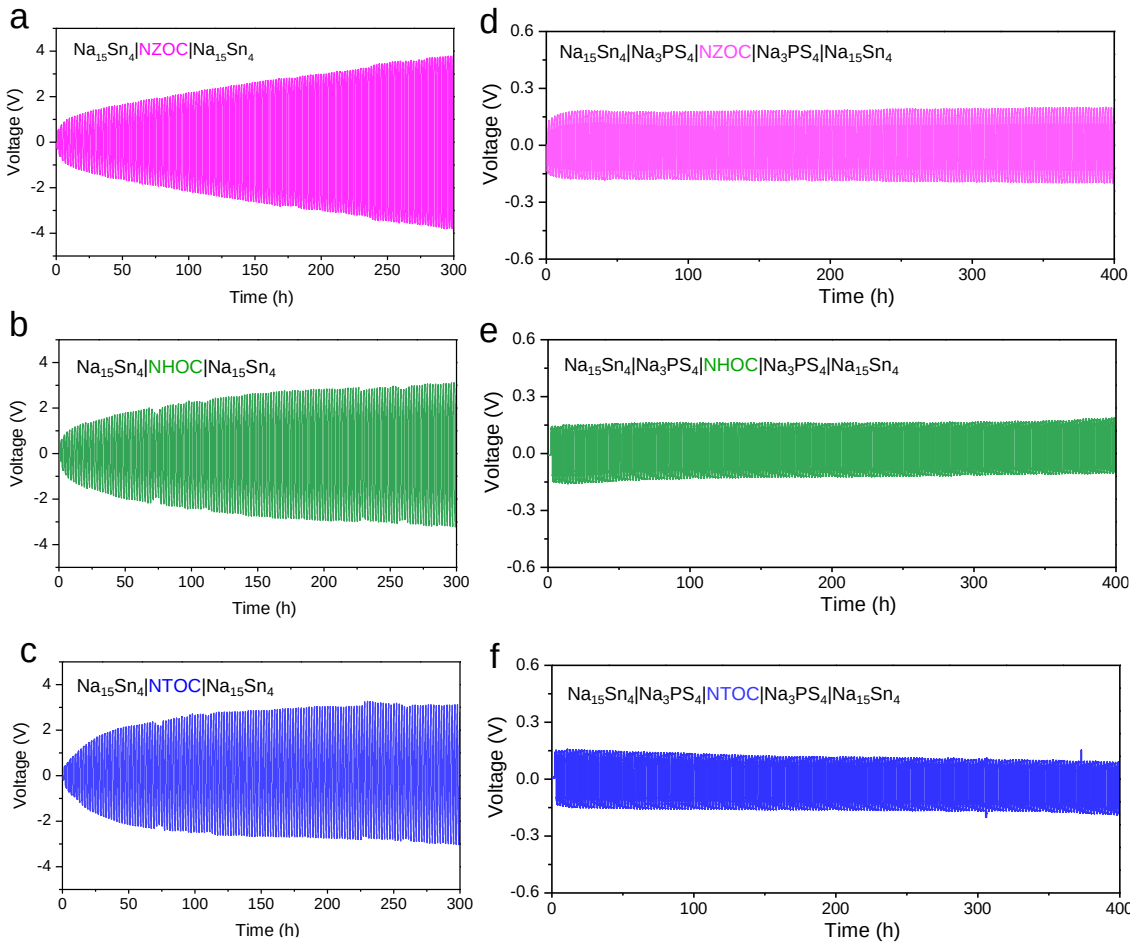

Supplementary Fig. 18. The cycling stability of (a-c) $Na_{15}Sn_4$/NMOC/$Na_{15}Sn_4$ and (d-f) $Na_{15}Sn_4$/Na_3PS_4/NMOC/Na_3PS_4/$Na_{15}Sn_4$ cells at 0.1 mA cm^{-2} and 0.1 mAh cm^{-2}, RT.

The significant increase in $Na_{15}Sn_4$/NMOC/$Na_{15}Sn_4$ cell overpotential during the plating/striping process further confirmed the formation of a non-passivating interface between NMOC SSEs and $Na_{15}Sn_4$ electrode. Fortunately, the interfacial incompatibility between NMOC SSEs and the $Na_{15}Sn_4$ anode can be addressed by introducing a Na_3PS_4 interlayer, which is promising to facilitate the stabilization of the electrolyte/anode interface in ASSNIBs.

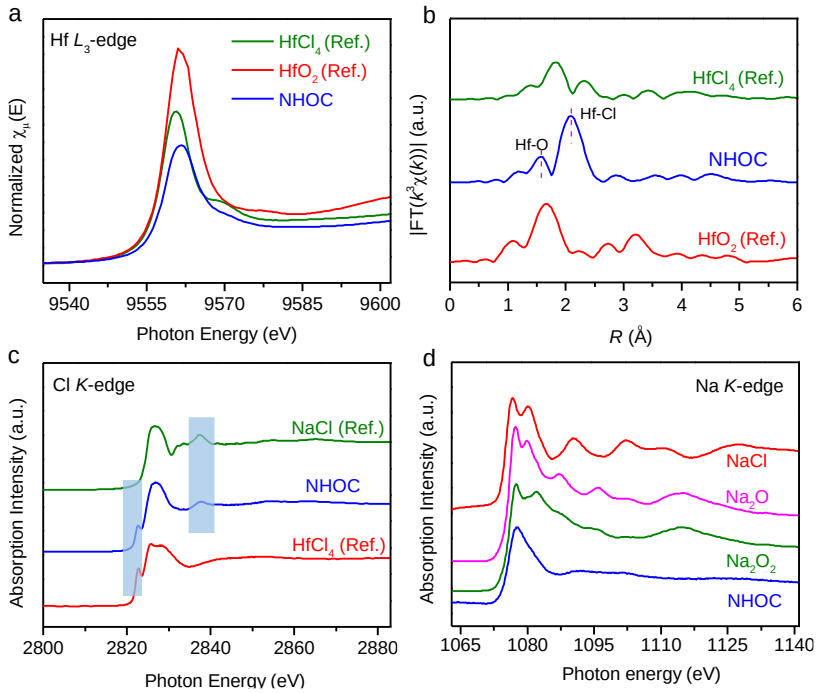

Supplementary Fig. 19. (a) Typical Hf *L*3-edge XANES spectra of the NHOC SSE and the references. (b) FT-EXAFS of Hf *L*3-edge for the NHOC SSE, HfO_2, and $HfCl_4$. The (c) Cl *K*-edge and (d) Na *K*-edge XAS spectra of NHOC and reference samples.

NHOC showed an E_0 positioned between $HfCl_4$ and HfO_2, suggesting different Hf binding state. Both Hf-O and Hf-Cl paths can be clearly observed in the FT-EXAFS spectra of Hf *L*3-edge for NHOC. The combination of Cl *K*-edge and Na *K*-edge XAS results suggested that Cl anions are weakly bonded with Na^+ in amorphous NHOC electrolyte, which benefits to high Na^+ mobility.

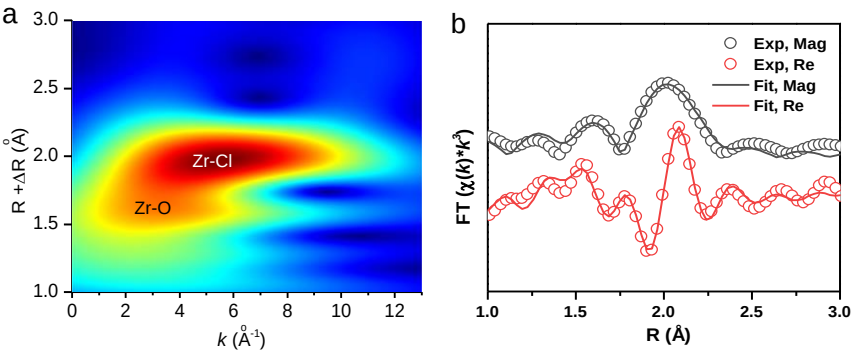

Supplementary Fig. 20. (a) The WT-EXAFS of NZOC electrolyte at Zr *K*-edge. A k^2 weighting was used. (b) FT-EXAFS fitting results for the Zr *K*-edge spectrum of the NZOC.

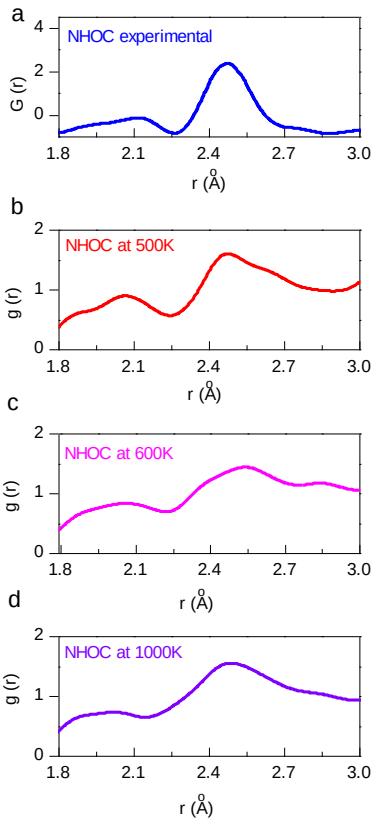

Supplementary Fig. 21. (a) Experimentally measured PDF profile of NHOC electrolyte. Calculated pair correlation functions (g (r)) of NHOC electrolyte at (b) 500 K, (c) 600 K, and (d) 1000 K.

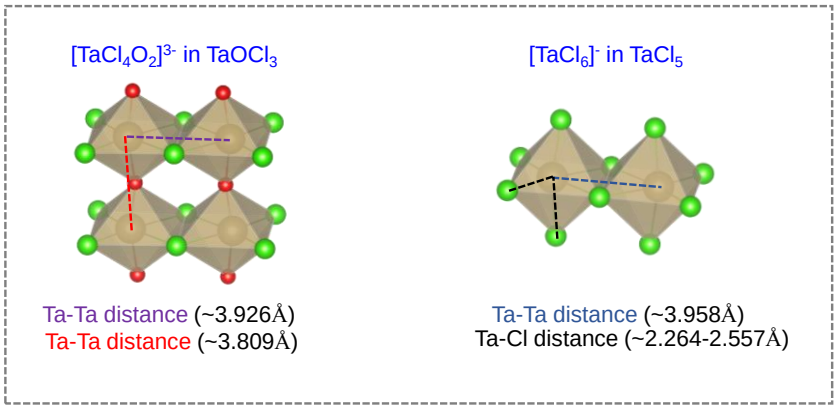

Supplementary Fig. 22. The Ta-Ta and Ta-Cl pair distance in the basic building blocks of $TaOCl_3$ and $TaCl_5$ references.

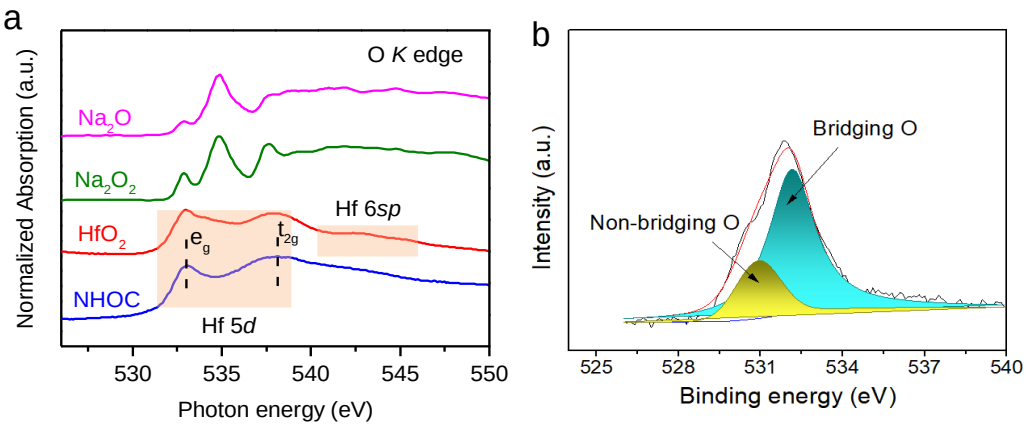

Supplementary Fig. 23. (a) The O *K*-edge spectrum of NHOC electrolyte and reference samples. (b) O 1s XPS spectrum of NHOC electrolyte.

The O *K*-edge spectra suggests that the chemical environment around O in NHOC should be similar to that of the monoclinic HfO_2. In other words, the O is mainly coordinated with Hf rather than Na. Additionally, both bridging and non-bridging oxygen exits in the NHOC electrolyte based on the O 1s XPS results.

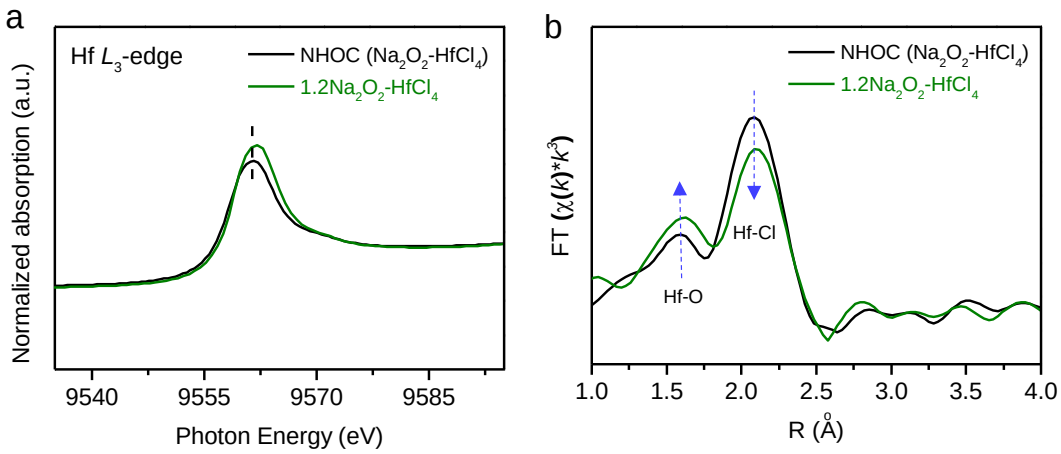

Supplementary Fig. 24. (a) XANES spectra and (b) FT-EXAFS spectra of the xNa_2O_2-$HfCl_4$ (x=1.0, 1.2) at Hf L_3-edge.

The as-prepared 1.2Na_2O_2-$HfCl_4$ compound are mixtures of crystalline NaCl impurity and an amorphous phase with rich O and less Cl around the centered-Hf, compared with that of the NHOC electrolyte.

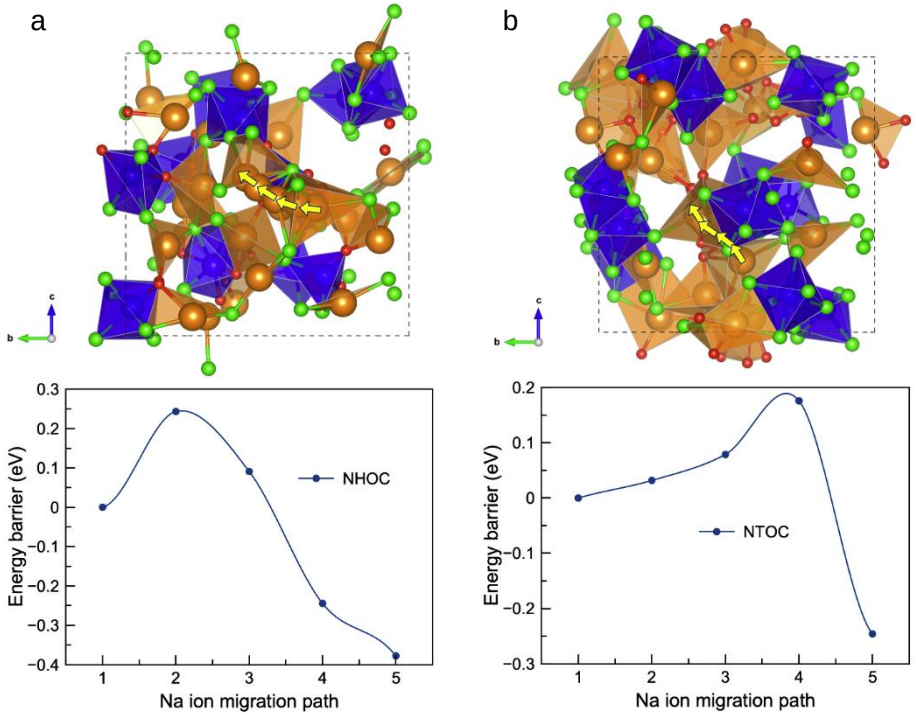

Supplementary Fig. 25. Na-ion migration pathway 1 (upper) and energy barrier (lower) in (a) NHOC (500K) and (b) NTOC (500K) electrolytes.

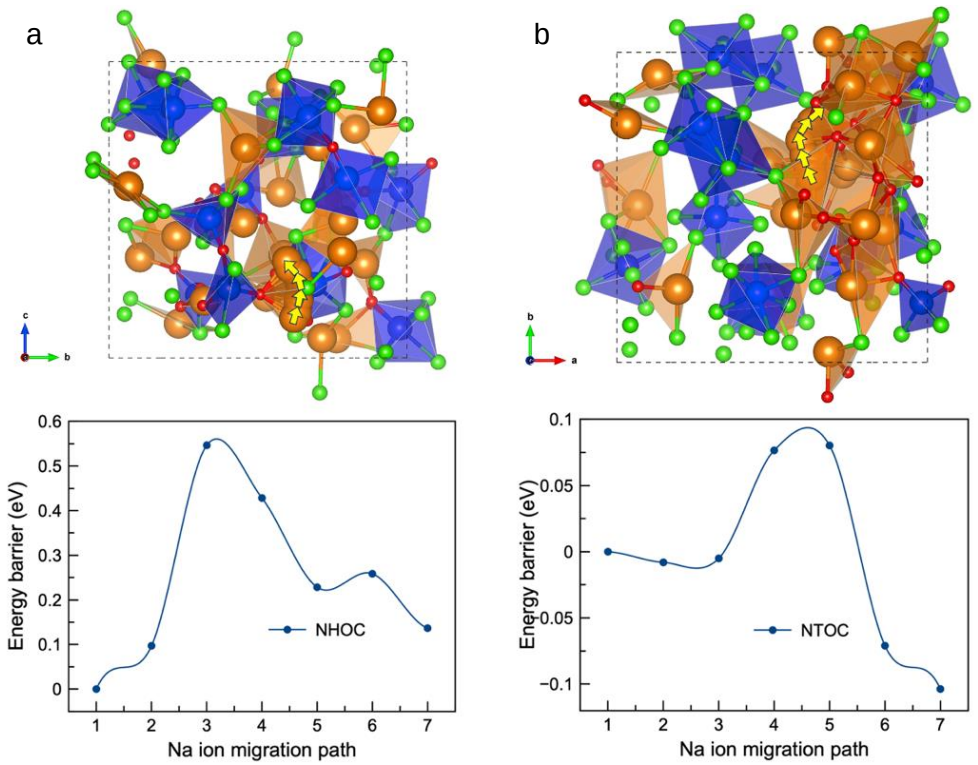

Supplementary Fig. 26. Na-ion migration pathway 2 (upper) and energy barrier (lower) in (a) NHOC (500K) and (b) NTOC (500K) electrolytes.

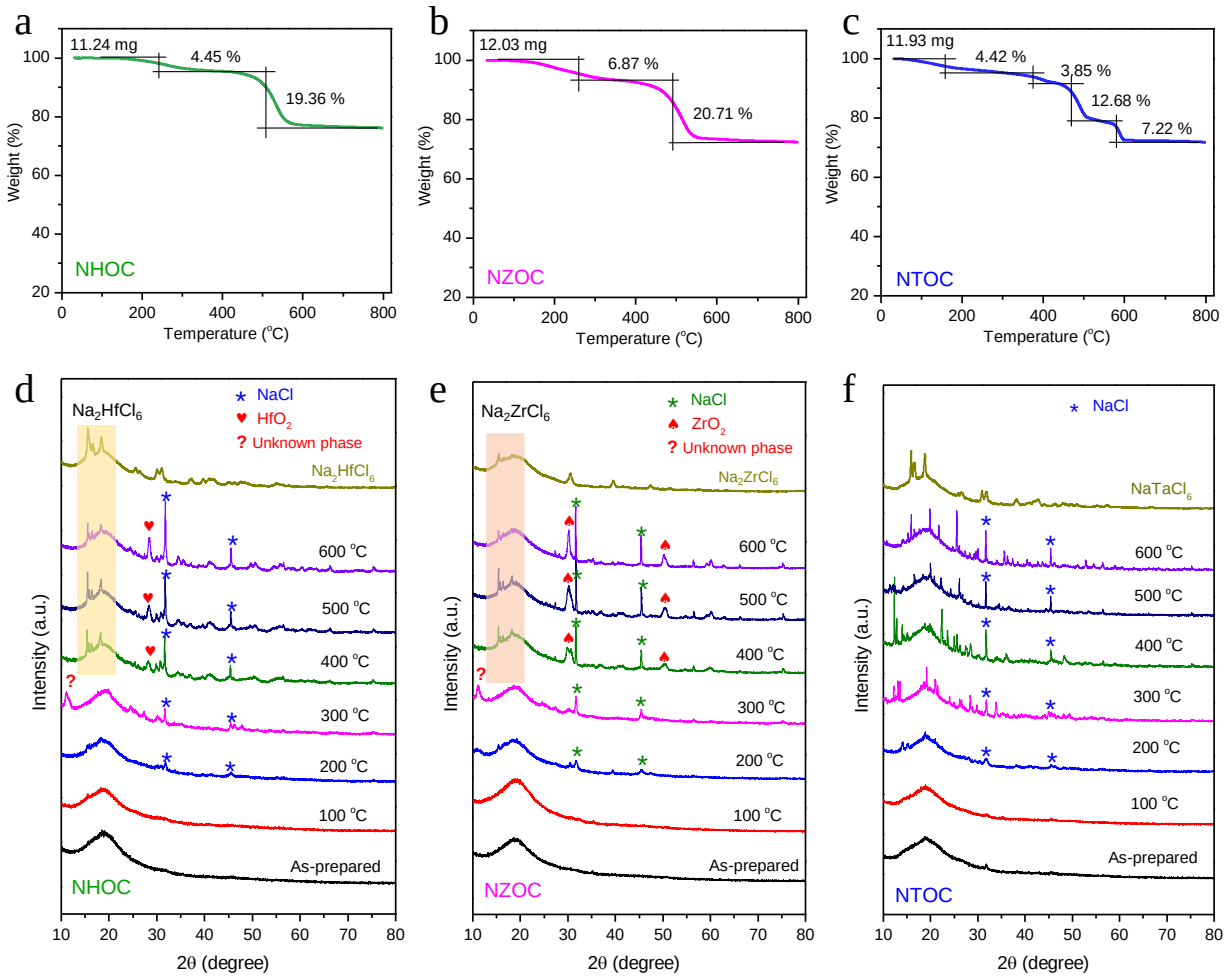

Supplementary Fig. 27. TGA curves of (a) NHOC, (b) NZOC, and (c) NTOC electrolytes. The XRD patterns of the (d) NHOC, (e) NZOC, and (f) NTOC after sintering at different temperatures under vacuum.

NHOC and NZOC electrolytes exhibit similar thermal stability up to ~180℃, and NTOC electrolyte has an intrinsic thermal stability up to ~130℃. The relative poor thermal stability of NTOC may be attributed to its intrinsic local structures with a large number of Ta-centered polyhedrons that are connected mainly via corner-sharing O, which are different from those of NHOC and NZOC, which are composed of M-centered polyhedrons connected via corner-sharing oxygen, edge-sharing oxygen, and edge-sharing chlorine. It is noted that NHOC and NZOC electrolytes show similar thermal stability, which is consistent with our structural analysis that shows that the local structures of NHOC and NZOC are of high similarity.

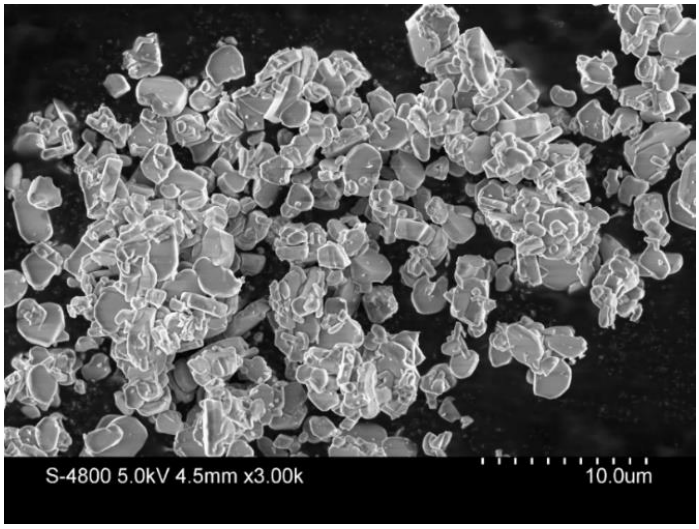

Supplementary Fig. 28. The SEM image of layered oxide NMNFO cathode.

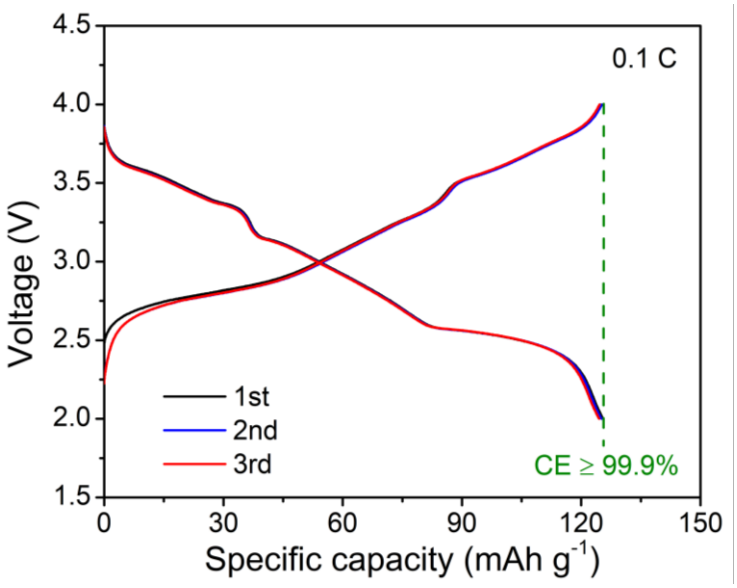

Supplementary Fig. 29. The discharge-charge profiles of NHOC-basedASSNIB at 0.1C, RT.

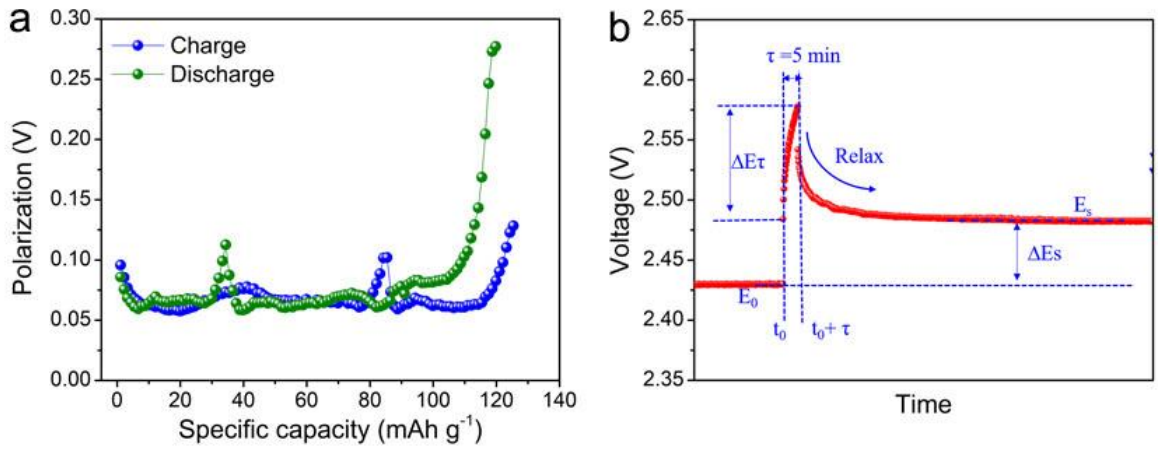

Supplementary Fig. 30. (a) The polarization plots obtained by GITT of NHOC-based ASSNIB at 0.1C. (b) Detailed voltage response during a single current pulse with time of ASSNIB.

The significant increase in polarization at ~3.3 V during charging can be attributed to the structural transition from O3-NMNFO to P3-NMNFO phases, and the significant increase in polarization at the end of the discharge process was partially due to the saturation of Na^+ sites in the NMNFO crystal structure. Additionally, the average apparent diffusion coefficient, D_{Na+}, of NMNFO in ASSNIB was 3.244×10^{-13} and 3.19×10^{-13} cm^2 S^{-1} during the initial charge and discharge processes, respectively.

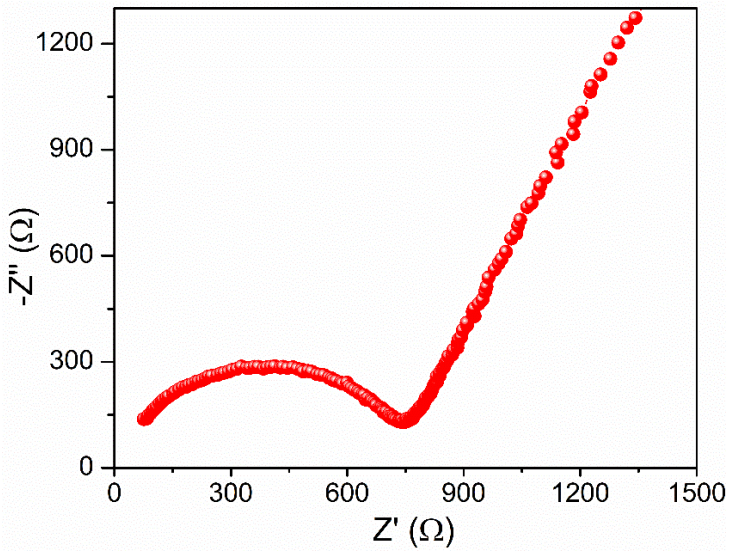

Supplementary Fig. 31. The Nyquist plot of as-prepared Na_3PS_4 electrolyte at RT.

The ionic conductivity of as-prepared Na_3PS_4 electrolyte is 1.2×10^{-4} S cm^{-1} at RT.

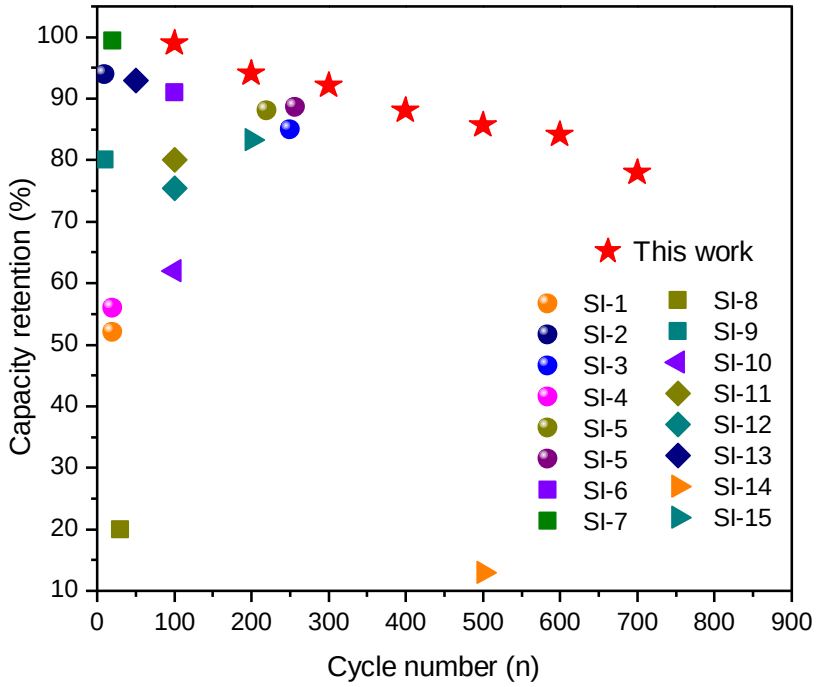

Supplementary Fig. 32. Comparison of this work with room-temperature all-solid-state sodium batteries from literatures.

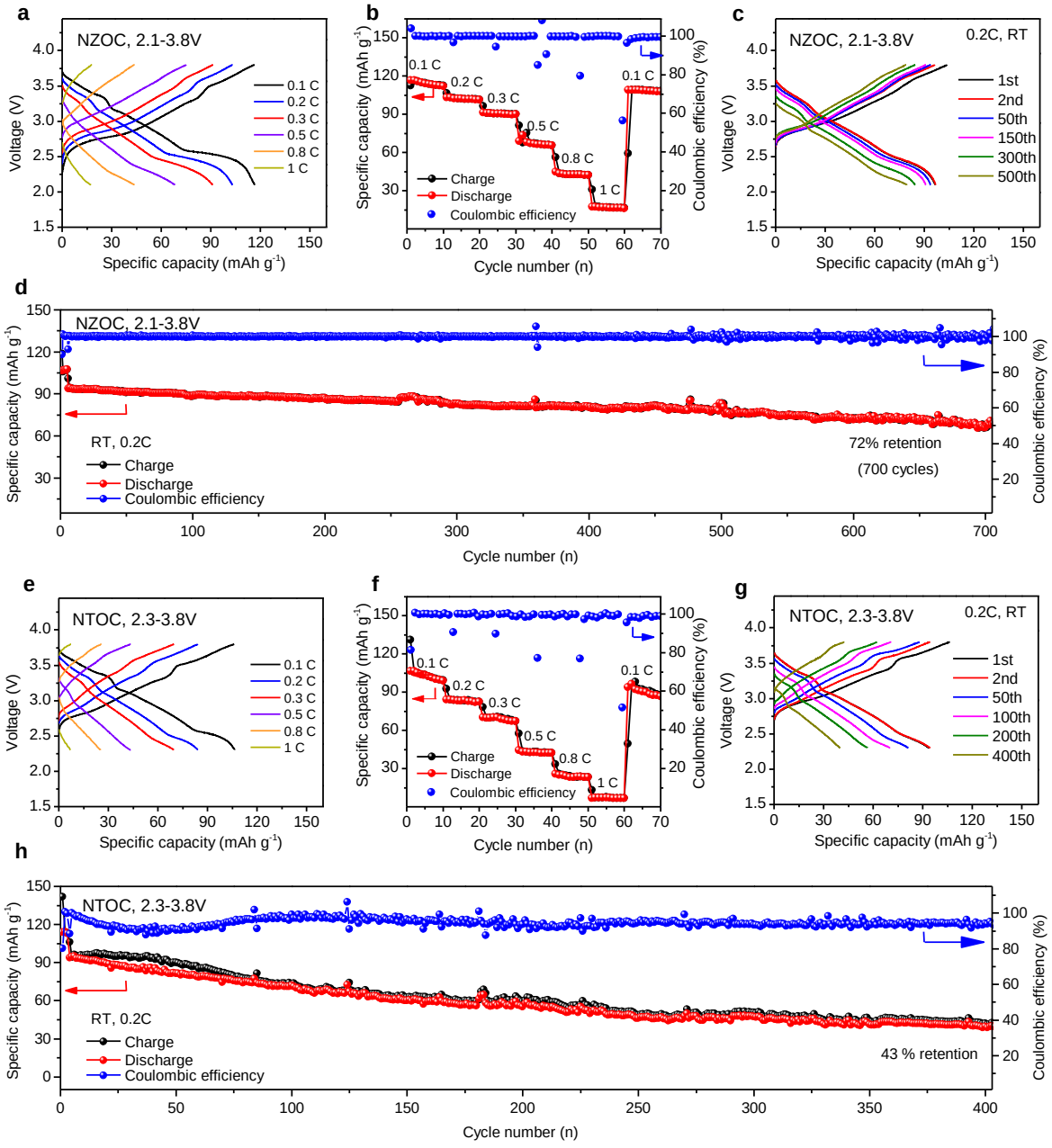

Supplementary Fig. 33. Electrochemical performance of NZOC- and NTOC-based ASSNIBs. (a) Charge/discharge curves and (b) rate capability of NZOC-based ASSNIB under various current densities at RT. (c) Galvanostatic voltage profiles and (d) specific capacity of NZOC-based ASSNIBs as a function of cycle number, respectively, running at 0.2C, RT. (e) charge/discharge curves and (f) rate capability of NTOC-based ASSNIB under various current densities at RT. (g) Galvanostatic voltage profiles and (h) specific capacity and Coulombic efficiency of NTOC-based ASSNIBs as a function of cycle number, respectively, running at 0.2C, RT.

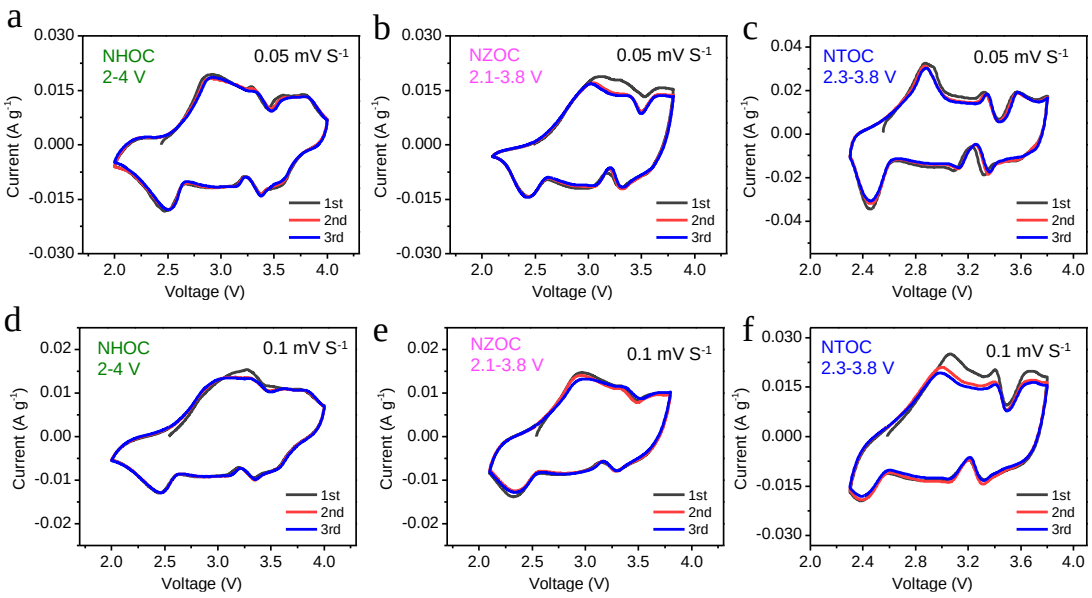

Supplementary Fig. 34. (a-c) The CV curves of NHOC-, NZOC-, and NTOC-based ASSNIBs at 0.05 mV S^{-1}. (d-e) The CV curves of NHOC-, NZOC-, and NTOC-based ASSNIBs at 0.1 mV S^{-1}.

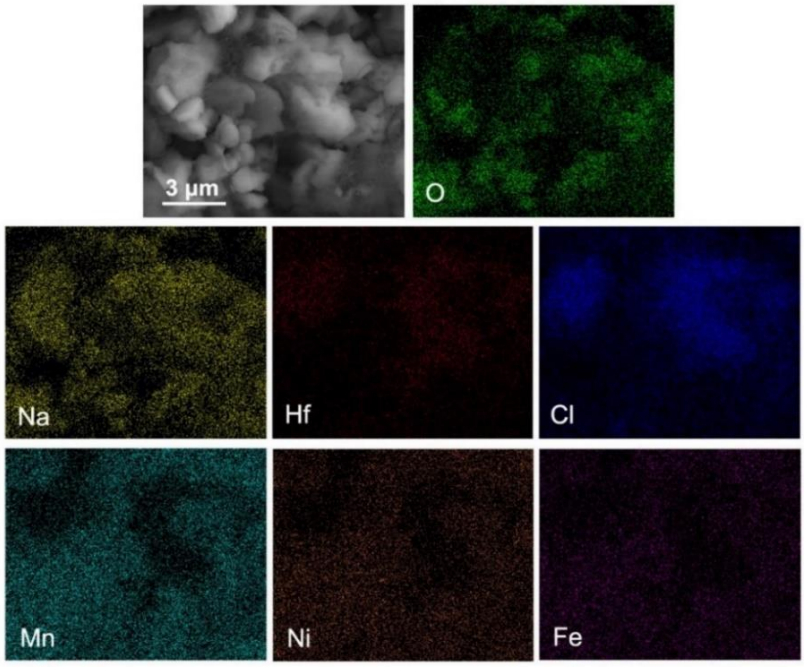

Supplementary Fig. 35. Cross-sectional SEM image and corresponding EDS mapping of the composite cathode for NHOC-based ASSNIB.

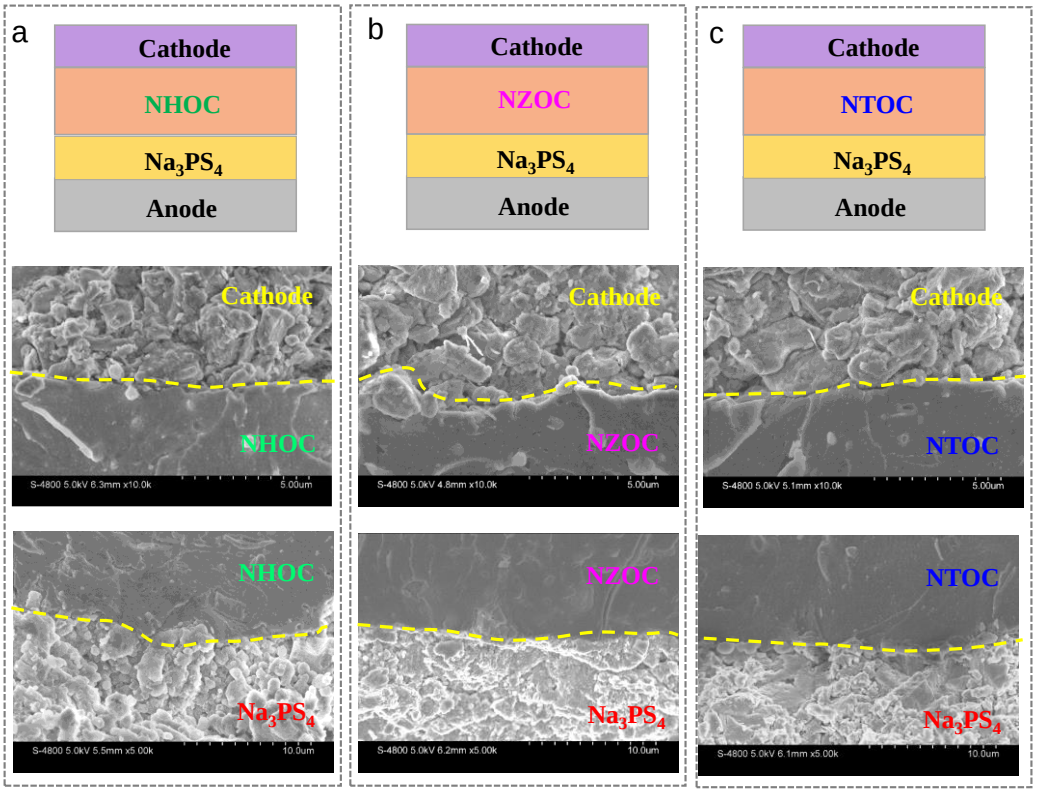

Supplementary Fig. 36. The Cross-sectional SEM images interfaces between different cell components in (a) NHOC-, (b) NZOC-, and (c) NTOC-based ASSNIB. The dotted yellow line showing the interfaces between different cell components.

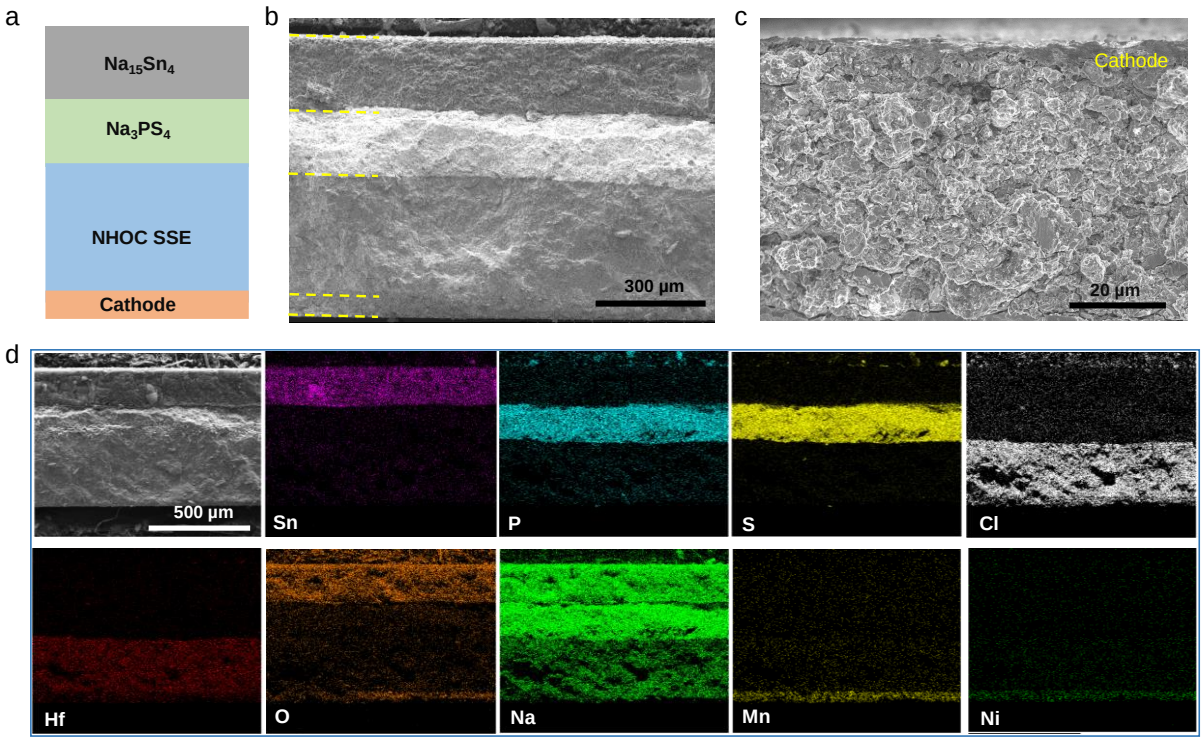

Supplementary Fig. 37. (a) Schematic illustration of a NHOC-based ASSNIB. Cross-sectional SEM image of (b) the ASSNIB and (c) the cathode layer. (d) SEM image and corresponding EDS mapping of the ASSNIB before cycling.

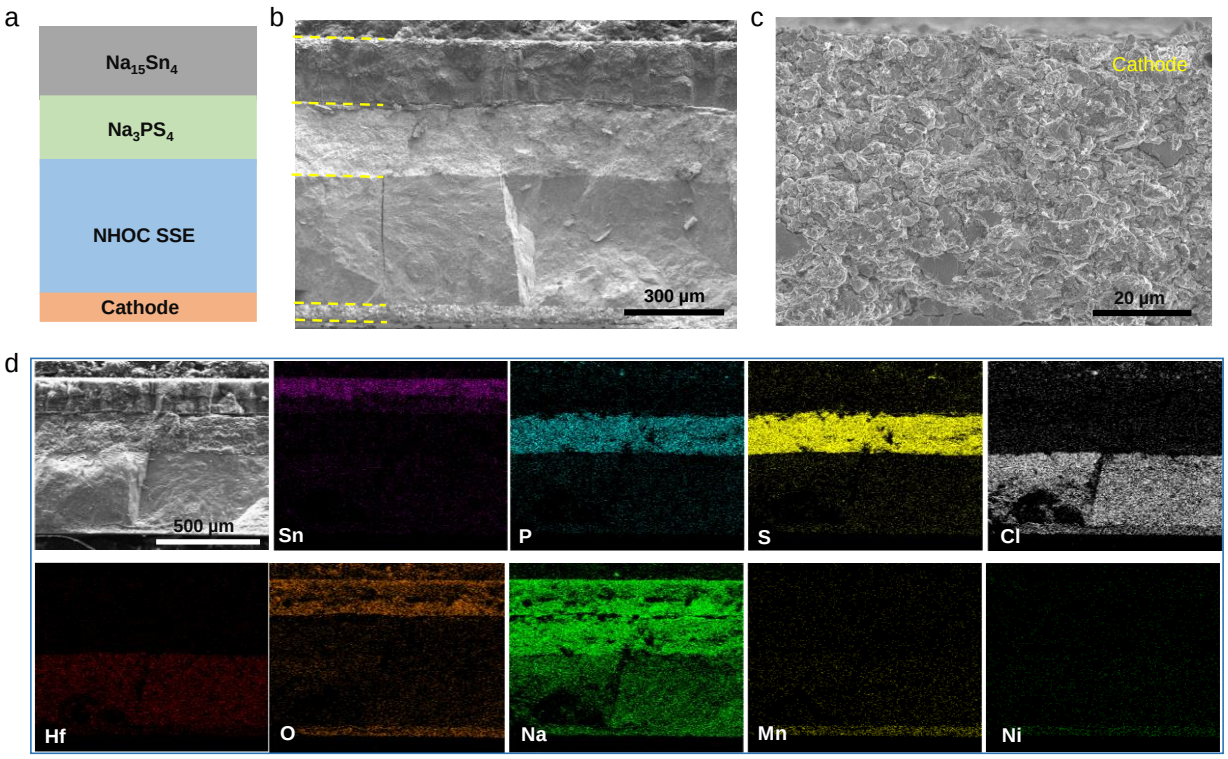

Supplementary Fig. 38. (a) Schematic illustration of NHOC-based ASSNIB. Cross-sectional SEM image of (b) the ASSNIB and (c) the cathode layer after cycling at 0.2C for 50 cycles. (d) SEM image and EDS mapping of the cross-section of ASSNIB after cycling at 0.2C for 50 cycles.

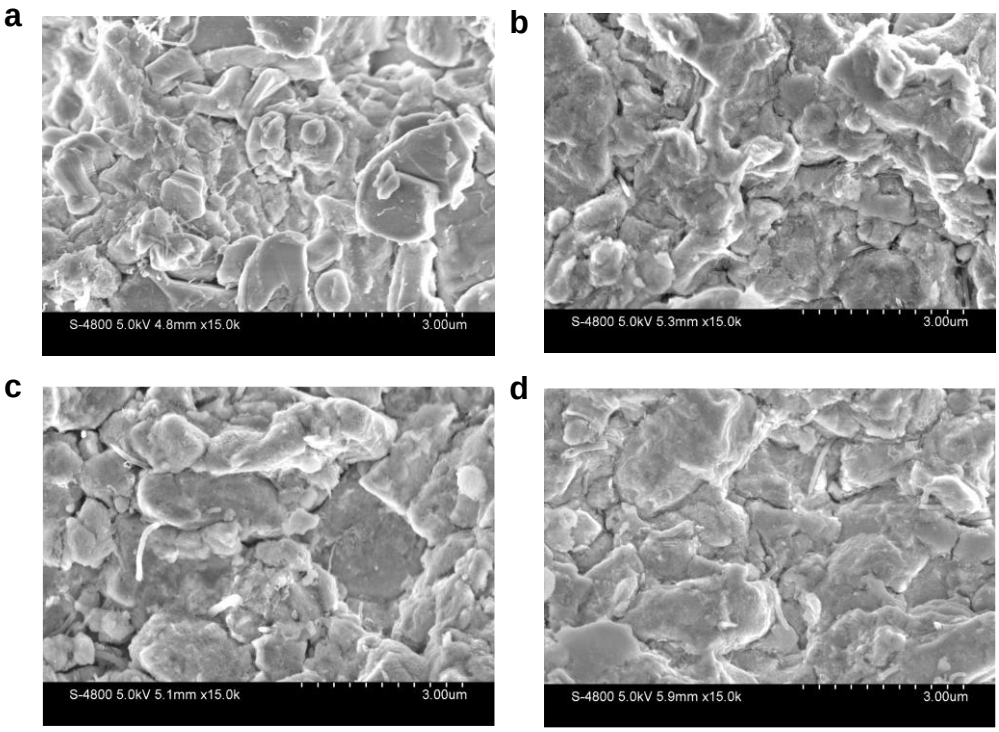

Supplementary Fig. 39. The cross-sectional SEM images of (a) pristine NHOC-based cathode electrode, and NHOC-based cathode electrode after (b) 1, (c) 20 and (d) 50 cycles.

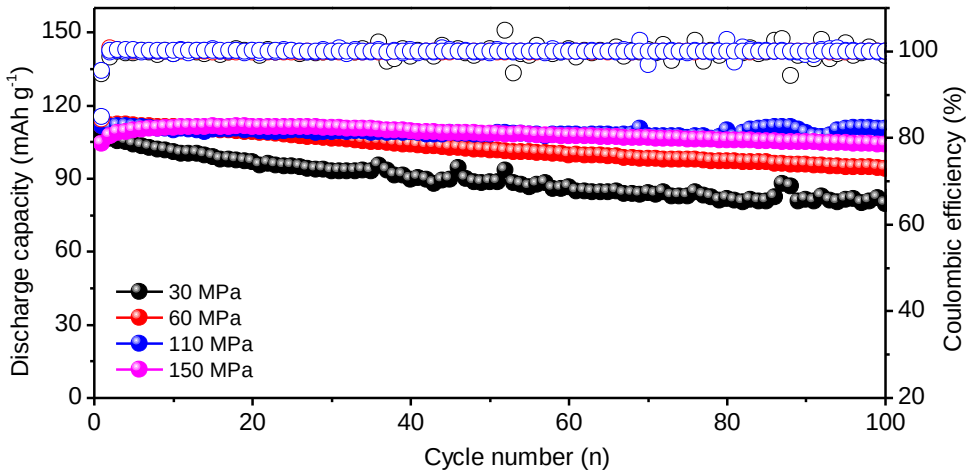

Supplementary Fig. 40. The effect of the operating stack pressure on the NHOC-based ASSNIBs' cycling performance at 0.2 C, RT.

The fluctuation of the cell discharge capacity at 30 MPa is due to temperature variation.

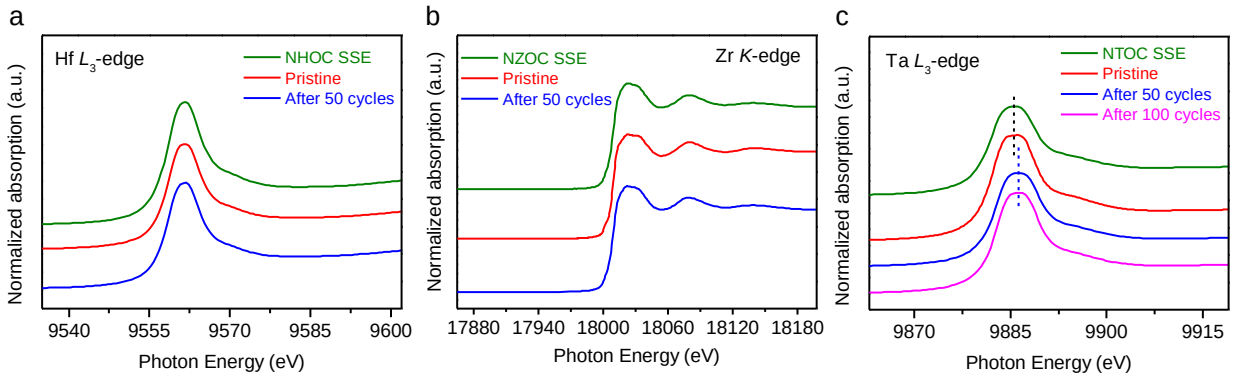

Supplementary Fig. 41. (a) Hf L_3-edge XANES spectra of NHOC-based cathode electrode before and after cycling. (b) Zr *K*-edge XANES spectra of NZOC-based cathode electrode before and after cycling. (c) Ta L_3-edge XANES spectra of NTOC-based cathode before and after cycling.

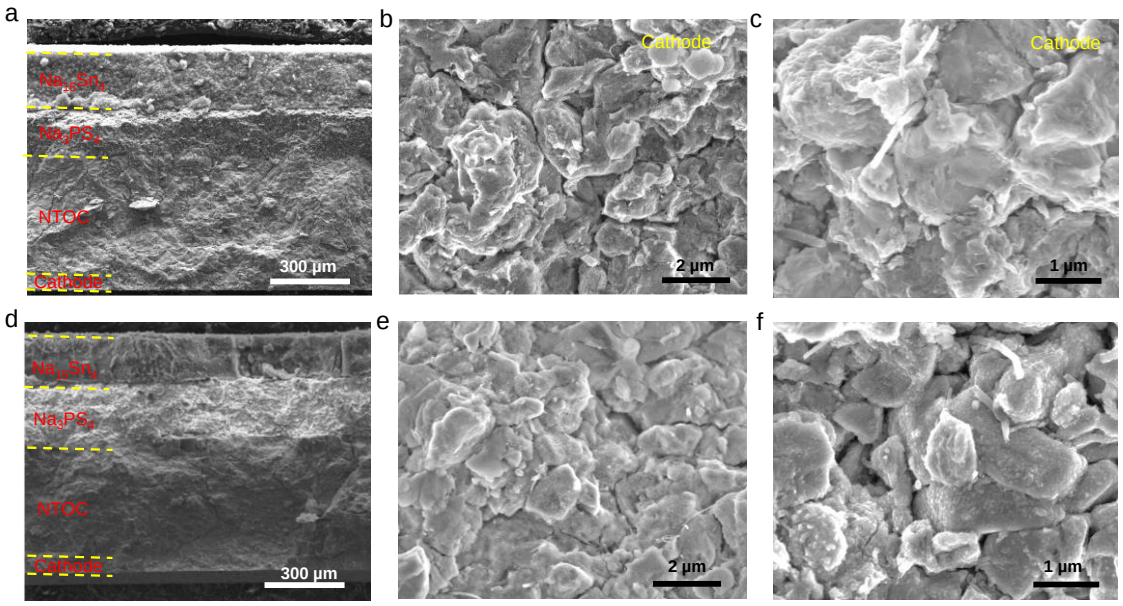

Supplementary Fig. 42. The cross-sectional SEM images of NTOC-based ASSNIB (a) before and (d) after 100 cycles. The SEM images of the NTOC-based cathode composite (b, c) before and (e, f) after 100 cycles.

The large cracks observed on both the pristine and cycled NTOC electrolyte result from external stress encountered during the cell disassembly process. The whole battery structure is basically preserved after cycling, without significant cell components delamination was observed. However, numerous unknown nano-sized byproducts appeared on the cathode surface after cycling, suggesting the occurrence of interfacial reactions between the NTOC and the NMNFO cathode.

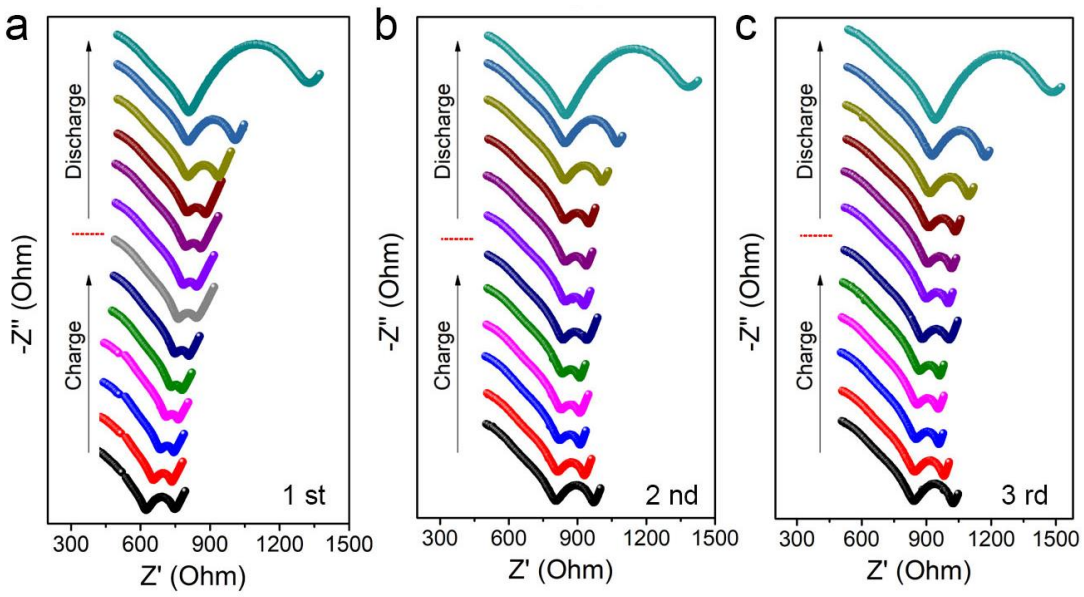

Supplementary Fig. 43. The EIS spectra of NHOC-based ASSNIB in the initial three cycles.

Supplementary Table 1. Refined crystal structure of Na_2HfCl_6. Crystallographic data of Na_2HfCl_6 based on synchrotron-based XRD data.

Compound	Na_2HfCl_6
Space group	*P2₁/n*
a, Å	6.6489(10)
b, Å	7.0543(9)
c, Å	9.7859(16)
α , °	90
β , °	92.342(12)
γ , °	90
V, $Å^3$	458.61(8)

Supplementary Table 2. Rietveld analysis results for the XRD pattern of Na_2HfCl_6.

Atom	x	y	z	Occ.	U	site	Sym.
Hf1	1/2	1/2	1/2	1	0.0216	2a	-1
Na2	0.54340	0.08340	0.22480	1	0.038	4e	1
Cl3	0.31470	0.16300	0.94040	1	0.024	4e	1
Cl4	0.12830	0.95600	0.22670	1	0.036	4e	1
Cl5	0.66790	0.78430	0.42810	1	0.038	4e	1

Supplementary Table 3. Refined crystal structure of $NaTaCl_6$. The cystallographic data of $NaTaCl_6$.

Compound	$NaTaCl_6$
Space group	$P2_1/c$
a, Å	6.4602(6)
b, Å	6.8845(5)
c, Å	19.0031(16)
α , °	90
β , °	90.794(8)
γ , °	90
V, $Å^3$	845.08(9)

Supplementary Table 4. Rietveld analysis results for the XRD pattern of $NaTaCl_6$.

Atom	x	y	z	Occ.	U	site	Sym.
Ta1	0.25660	0.21720	0.11354	1	0.026	4e	1
Cl1	0.37880	0.20590	0.23340	1	0.039	4e	1
Cl2	0.55020	0.39710	0.09390	1	0.046	4e	1
Cl3	0.09730	0.49730	0.16060	1	0.037	4e	1
Cl4	0.11030	0.24490	0.00530	1	0.047	4e	1
Cl5	-0.05440	0.04990	0.14560	1	0.035	4e	1
Cl6	0.42370	-0.07550	0.09710	1	0.047	4e	1
Na1	0.81000	0.28300	0.24430	1	0.055	4e	1

Supplementary Table 5. The specific densities of NMOC SSEs measured by True Density Meter.

Solid state electrolyte	Specific density (g cm^{-3})
NHOC	3.01
NZOC	2.57
NTOC	2.96

Supplementary Table 6. Structural parameters of amorphous NHOC electrolyte obtained from the Hf L_3-edge EXAFS fittings.

	CN	d (Å)	σ^2 (Å^2)
Hf-O path	2.3 ± 0.4	2.04 ± 0.02	0.006 ± 0.000
Hf-Cl path	3.5 ± 0.6	2.46 ± 0.01	0.005 ± 0.002

*CN, coordination number; d (Å), bonding distance; σ^2, Debye-Waller factor. ΔE_0 is the inner potential correction. The S_0^2 was fixed as 0.82. ΔE_0 is 4.6 eV. R factor for this fitting is 0.015. The fitted *k* range was set to be 3-13 Å^{-1}, and the fitted R range was set to be 1-2.65 Å. A k^2 weighting was used.

Supplementary Table 7. Structural parameters of amorphous NZOC electrolyte obtained from the Zr *K*-edge EXAFS fittings.

	CN	d (Å)	σ^2 (Å^2)
Zr-O path	1.9 ± 1.3	2.08 ± 0.04	0.004 ± 0.006
Zr-Cl path	3.8 ± 0.5	2.48 ± 0.01	0.004 ± 0.001

*CN, coordination number; d (Å), bonding distance; σ^2, Debye-Waller factor. ΔE_0 is the inner potential correction. The S_0^2 was fixed as 0.79. ΔE_0 is 1.2 eV. R factor for this fitting is 0.038. The fitted *k* range was set to be 2.5-14 Å^{-1}, and the fitted R range was set to be 1.1-2.8 Å. A k^2 weighting was used.

Supplementary Table 8. Structural parameters of amorphous NTOC electrolyte obtained from the Ta L_3-edge EXAFS fittings.

	CN	d (Å)	σ^2 (Å^2)
Ta-O path	2.0 ± 0.5	1.84 ± 0.01	0.003 ± 0.002
Ta-Cl path	3.6 ± 0.7	2.35 ± 0.01	0.004 ± 0.002

*CN, coordination number; d (Å), bonding distance; σ^2, Debye-Waller factor. ΔE_0 is the inner potential correction. The S_0^2 was fixed as 0.81. ΔE_0 is 0.05 eV. R factor for this fitting is 0.068.

The fitted *k* range was set to be 3-13 $Å^{-1}$, and the fitted R range was set to be 1.1-2.8 Å. A k^2 weighting was used.

Supplementary Table 9. Cycling performance of all-solid-state sodium batteries reported in **Supplementary Fig. 33**.

Cathode types	Material	Current density	Cycles (n)	Capacity retention (%)	Testing temperature (℃)	Reference	
Layered oxide	NMNFO	0.2 C	100	99%	RT	**This work**	
			200	94.1%			
			300	92.1%			
			400	88.1%			
			500	85.7%			
			600	84.1%			
			700	78%			
	$NaCrO_2$	~0.14 C (1C=175 mA/g)	20	~52	RT	***Electrochimica Acta** 2018*, 259, 100-109	SI-1
	$NaCrO_2$	0.05 C	10	94	RT	***Electrochemistry Communications*** 2019, 106, 106534,	SI-2
	$NaCrO_2$	0.2 C	250	85	RT	***Energy & Environmental Science***, 2017, 10, 2609-2615	SI-3
	$NaCrO_2$	~0.05 C	20	~56	30	***Angewandte Chemie International Edition**, 2016*, 55, 9634-9638	SI-4
	$NaCrO_2$	0.5C	220	88.1	20	***Nature Communications*** 2021, 12, 1256,	SI-5
		0.1C	257	88.6	20		
Metal sulfide	TiS_2	0.11 C (1C = 198 mA/g)	100	~91	30	***ACS Energy Letters**, 2018*, 3, 2504-2512,	SI-6
	TiS_2	0.24 C	20	99.4	30	***Advanced Energy Materials**, 2018*, 8, 1702716	SI-7
	TiS_2	0.05 C	30	20	RT	***Advanced Functional Materials***, 2020, 30, 2001118.	SI-8
	TiS_2	0.1 C	10	80	RT	***Scientific Reports**, 2016*, 6, 33733.	SI-9
	MoS_2	0.05 C (1C=670 mA/g)	100	~62	RT	***The Journal of Physical Chemistry C**, 2020*, 124, 10298-10305.	SI-10

	FeS_2	0.07 C (1C=894 mA/g)	100	80	RT	***ACS Applied Materials & Interfaces***, *2018*, 10, 12300-12304	SI-11
	$Fe_{1-x}S$	0.16 C (1C=610 mA/g)	100	75.45	RT	***ACS Nano***, *2018*, 12, 2809-2817	SI-12
Elemental	S	0.048 C (1C=1677 mA/g)	50	93	RT	***Electrochemistry Communications***, 2020, 116, 106741	SI-13
	Sn-Se	0.2 C	500	~13	RT	***Journal of Materials Chemistry A***, 2019, 7, 20790-20798	SI-14
Prussian Blue	$Na_2MnFe(CN)_6$	0.2 C	200	83.3	RT	***Advanced Functional Materials***, *2021*, 31, 2002144	SI-15

Reference

1 Liang, F. *et al.* Cobalt-doped $TaOCl_3$ nanoparticles/carbon compounds with advanced specific capacity for lithium-ion batteries. *Journal of Alloys and Compounds* **897**, 163193, doi:https://doi.org/10.1016/j.jallcom.2021.163193 (2022).

2 Kwak, H. *et al.* Na_2ZrCl_6 enabling highly stable 3 V all-solid-state Na-ion batteries. *Energy Storage Materials* **37**, 47-54, doi:https://doi.org/10.1016/j.ensm.2021.01.026 (2021).